

Electronic Theses and Dissertations, 2004-2019

2014

Distribution of Laser Induced Heating in Multi-Component Chalcogenide Glass and its Associated Effects

Laura Sisken
University of Central Florida

 Part of the [Electromagnetics and Photonics Commons](#), and the [Optics Commons](#)
Find similar works at: <https://stars.library.ucf.edu/etd>
University of Central Florida Libraries <http://library.ucf.edu>

This Masters Thesis (Open Access) is brought to you for free and open access by STARS. It has been accepted for inclusion in Electronic Theses and Dissertations, 2004-2019 by an authorized administrator of STARS. For more information, please contact STARS@ucf.edu.

STARS Citation

Sisken, Laura, "Distribution of Laser Induced Heating in Multi-Component Chalcogenide Glass and its Associated Effects" (2014). *Electronic Theses and Dissertations, 2004-2019*. 4506.
<https://stars.library.ucf.edu/etd/4506>

DISTRIBUTION OF LASER INDUCED HEATING IN MULTI-COMPONENT
CHALCOGENIDE GLASS AND ITS ASSOCIATED EFFECTS

by

LAURA SISKEN

B.S. Missouri University of Science and Technology, 2012

A thesis submitted in partial fulfillment of the requirements

for the degree of Master of Science

in the College of Optics and Photonics

at the University of Central Florida

Orlando, FL

Spring Term

2014

Major Professor: Kathleen Richardson

©2014 Laura Siskin

ABSTRACT

Chalcogenide glasses are well known to have good transparency into the infrared spectrum. These glasses though tend to have low thresholds as compared to oxide glasses for photo-induced changes and thermally-induced changes. Material modification such as photo-induced darkening, bleaching, refractive index change, densification or expansion, ablation of crystallization have been demonstrated, and are typically induced by a thermal furnace-based heat treatment, an optical source such as a laser, or a combination of photo-thermal interactions. Solely employing laser-based heating has an advantage over a furnace, since one has the potential to be able to spatially modify the materials properties with much greater precision by moving either the beam or the sample.

The main properties of ChG glasses investigated in this study were the light-induced and thermally-induced modification of the glass through visible microscopy, white light interferometry, and Raman spectroscopy. Additionally computational models were developed in order to aid in determining what temperature rise should be occurring under the conditions used in experiments.

It was seen that ablation, photo-expansion, crystallization, and melting could occur for some of the irradiation conditions that were used. The above bandgap energy simulations appeared to overestimate the maximum temperature that should have been reached in the sample, while the below bandgap energy simulations appeared to underestimate the maximum temperature that should have been reached in the sample. Ultimately, this work produces the ground work to be able to predict and control dose, and therefore heating, to induce localized crystallization and phase change.

TABLE OF CONTENTS

LIST OF FIGURES	vi
LIST OF TABLES	x
LIST OF ACRONYMS	xi
1 INTRODUCTION.....	1
1.1 Chalcogenides – Use As Optical Materials	1
1.2 Chalcogenide Based Glasses and Glass Ceramics.....	1
1.3 Photo-induced Processes.....	5
2 RESEARCH OVERVIEW.....	9
2.1 Objectives and Goal.....	11
2.2 Computational Tools.....	11
2.3 Experimental Tools.....	12
2.4 Expected Outcomes	12
3 COMPUTATIONAL TECHNIQUES.....	14
3.1 Semi-infinite Material Approximation	16
3.2 Finite Boundary Model.....	18
3.3 Pulsed Laser Experiments.....	20
3.4 Comparison of Models.....	24
3.5 Summary.....	26

4	EXPERIMENTAL VALIDATION OF COMPUTATIONAL MODELS	28
4.1	Above Bandgap Energy	28
4.2	Below Bandgap Energy Radiation.....	29
4.3	Threshold Mapping.....	32
4.4	Characterization of Material Property Changes.....	37
4.5	Summary.....	47
5	COMPARISON OF COMPUTATIONAL TECHNIQUES WITH EXPERIMENTS ..	49
5.1	Comparison of Calculated Temperatures with Observed Material Changes.....	49
5.2	Differences in Deviation for Above and Below Bandgap	56
5.3	Summary.....	57
6	CONCLUSION	58
6.1	Future Work.....	59
	APPENDIX A: IRG-24 DATA SHEET FROM SCHOTT GLASS	61
	APPENDIX B: DOSAGES FOR THRESHOLD MAPPING	64
	REFERENCES	70

LIST OF FIGURES

- Figure 1 The representative rates of nucleation and crystallization are plotted against temperature, where I is the nucleation curve and U is the growth curve..... 3
- Figure 2 On the left is a base glass, which has a volume fraction of 100% of glass. The center picture shows a nucleated sample, which is base glass that has been heat treated at a temperature where nucleation can occur. The glass at this point has a volume fraction of glass, V_g , which is 100% minus a small amount due to the finite volume of the crystal nuclei, V_x . The right picture is of a grown sample, where a nucleated sample is subsequently subjected to a heat treatment where crystal growth occurs. The V_g is now 100% minus 10-20% V_x , as was used in this study. 4
- Figure 3 Laser irradiation should also be able to grow crystallites from a base or nucleated sample into a grown sample. The spatial extent and location of the growth would be controllable in this situation, which could lead to spatially modified material properties of a glass..... 5
- Figure 4 Shown is the heat flow measured from a DSC, where the inflection point on the left side of the dip around 200°C is the T_g of the glass, and the onset of the peak just past 240°C is the T_x of the glass 10
- Figure 5 A representative UV-VIS absorption curve of a representative chalcogenide glass that is compositionally similar to the glasses used in this study 14
- Figure 6 For the semi-infinite boundary approximation, the material “extends to infinity” in all directions except for the surface incident to the laser irradiation. This leads to no heat transfer at the boundaries that extend to infinity, and a negligible amount that leaves the incident surface. 17
- Figure 7 (a) Geometry used to describe the finite boundary condition as the laser beam hits the first planar input face of the glass surface, and (b) illustration of convective heat flux is able to leave the sample in all directions. 19
- Figure 8 The maximum temperature obtained for simulations of 100 pulses of 2 μ m light was plotted against the heat transfer coefficient. There is only a small variation in the maximum temperature reached across this range. 20
- Figure 9 A schematic illustrating the temperature increase from individual laser pulses are plotted offset from each other. It can be seen that a temperature rise can start to occur for later pulses before the heat from previous pulses is able to dissipate completely if there is not enough time for the temperature to decay back to its original position. This leads to heat accumulation in the sample over many pulses. 21

Figure 10 Sampling rates for a larger value for the pulse divider (A), and a smaller pulse divider (B). The time between sampling is defined as the pulse FWHM divided by a certain value which is defined as the pulse divider. As can be seen the larger the pulse divider, the closer the sampled function is to the actual input function..... 22

Figure 11 The maximum attained temperatures for different values of the pulse divider are plotted above for one pulse on the left, and two pulses on the right. As can be seen there is a large dependence of the maximum attained temperature on the pulse divider. 23

Figure 12 The maximum attained temperature is plotted against the pulse divider for different tolerances. (A) depicts a relative tolerance of 1E-9 for 20 pulses, (B) depicts a relative tolerance of 1E-6 for 20 pulses, (C) depicts a relative tolerance of 1E-9 for 200 pulses, and (D) depicts a relative tolerance of 1E-3 for 20 pulses. As can be seen, there is much less dependence of the maximum temperature on the pulse divider. There is through an associated uncertainty in the calculation that can be observed..... 24

Figure 13 The percent difference in maximum temperature reached between the semi-infinite and infinite boundary models is plotted against a normalized heating spot size that is defined as two times the beam waist divided by the diameter of the sample. There is a clear trend of deviation that can be seen as the size of the laser beam is increase since the infinite boundary approximation becomes invalid. At small beam sizes the finite boundary model is not able to properly solve the equations due to the finite size of the meshing used in the simulation. From [39]. 25

Figure 14 The laser setup that was used in the above bandgap exposures is shown. A 488nm laser was expanded and then hit the sample that was held in a vertical position. 29

Figure 15 The laser setup that was used in the below bandgap exposures is shown. The 2 μ m laser starts with a seed laser in an oscillator. This then goes through a pulse picker to be able to have different repetition rates. This then goes into a thulium doped fiber and is amplified again. The output from this is brought vertically off of the table in order to be able to have a sample in a flat position, since this set-up is used for various other machining experiments..... 30

Figure 16 The arrays that were used in the focused experiments are shown where 10x10 individual spots were exposed for 2 s each. Multiple arrays were exposed near each other with a different incident power level applied to each array..... 31

Figure 17 For the threshold experiments the laser focus was varied vertically. The horizontal blue line represents the beam waist, and the two green lines represent the Raleigh range of the beam..... 33

Figure 18 The threshold map for the base glass is shown. The vertical lines correspond to different power levels, while the horizontal lines correspond to different heights of the

focus. The squares correspond to different timescales used. The purple circles correspond to locations where expansion was observed.	34
Figure 19 The threshold map for the nucleated glass is shown. The vertical lines correspond to different power levels, while the horizontal lines correspond to different heights of the focus. The squares correspond to different timescales used. The purple circles correspond to locations where expansion was observed.	35
Figure 20 The threshold map for the grown glass is shown. The vertical lines correspond to different power levels, while the horizontal lines correspond to different heights of the focus. The squares correspond to different timescales used. The purple circles correspond to locations where expansion was observed.	36
Figure 21 Various material changes can be seen from a visible microscope including ablation with one or more halos, thermal stress fractures, and small melt pools.	39
Figure 22 Crystallization was observed around various ablation craters. The bar in the micrographs is 20 microns.	40
Figure 23 Visible and white light interferometer images are side by side for examples of expansion that was observed in the grown samples. The purple circles mark the area that was exposed.	41
Figure 24 Visible and white light interferometer images are side by side for examples of expansion that was observed in the nucleated samples. The purple circles mark the area that was exposed.	42
Figure 25 Visible and white light interferometer images are side by side for examples of expansion that was observed in the base samples. The purple circles mark the area that was exposed.	42
Figure 26 The Raman spectra for the wide area exposures is shown. The upper left is for base, the upper right is for nucleated, and the lower right is for the grown samples. The lines for A-D are representative of the different power levels the samples were exposed to, and their values are shown in the bottom left.	43
Figure 27 The peak heights for the Raman peaks identified in table 6 are plotted against the incident power levels. The blue lines are from the base glass, the green are from the grown glass, and the red are from the nucleated glass.	45
Figure 28 Visible microscopy and white light interferometry are shown for the focused exposures with the grown sample on the left, the nucleated sample in the middle, and the base sample on the right. No expansion is observed for any of the arrays, but ablation is seen for the highest power level in the grown and nucleated samples.	46

Figure 29 White light interferometry for the above bandgap irradiation experiments is shown for 500mW and 450mW exposures. Upper right image from [39].	47
Figure 30 The temperature from simulations after 100s is shown for the 500mW (top row) and 450mW (bottom row) for the axially-symmetric and 3D simulations.....	50
Figure 31 The maximum temperature for the different average incident powers for the wide area exposures is plotted. As can be seen there is a very small increase from the initial temperature of 293.13K.	52
Figure 32 The maximum temperature reached for different z-positions of the focus of the laser for the threshold exposures is plotted for an incident power of 30mW on the left, and 40mW on the right.	53
Figure 33 The maximum temperatures for variations in beam waist (top left), incident power (top right), thermal conductivity (middle left), heat capacity (middle right), and density (bottom left) are plotted for the above bandgap case. As can be seen the thermal conductivity and beam waist appear to have larger effects than the other parameters on the maximum temperature reached.	54
Figure 34 The maximum temperature for variations in the reflection coefficient (A), thermal conductivity (B), heat capacity (C), and density (D) are plotted for the below bandgap case. Of these the density has the least impact on the final attained temperature.	55
Figure 35 Schott data sheet for IRG 24. http://www.schott.com/advanced_optics/english/download/schott-infrared-chalcogenide-glasses-irg24-october-2013-eng.pdf	62
Figure 36 Schott data sheet for IRG 24. http://www.schott.com/advanced_optics/english/download/schott-infrared-chalcogenide-glasses-irg24-october-2013-eng.pdf	63

LIST OF TABLES

Table 1 Glass properties that were used in the various simulations, and where these values came from. See appendix A for the IRG-24 data sheet.....	15
Table 2 The maximum and minimum dosages for the different exposure times overall and for the irradiated areas that saw damage is shown for the base glass. The dosages were calculated assuming the focus was at the surface of the sample in the middle of the vertical distance that was traveled.	34
Table 3 The maximum and minimum dosages for the different exposure times overall and for the irradiated areas that saw damage is shown for the nucleated glass. The dosages were calculated assuming the focus was at the surface of the sample in the middle of the vertical distance that was traveled.	35
Table 4 The maximum and minimum dosages for the different exposure times overall and for the irradiated areas that saw damage is shown for the grown glass The dosages were calculated assuming the focus was at the surface of the sample in the middle of the vertical distance that was traveled.	37
Table 5 Characterization tools used for each experiment and what information can be obtained from each of them.	38
Table 6 Assignments to Raman peaks that were monitored for the normalized results.	44
Table 7 Dosages for base glass threshold map in <i>Jscm2</i> . The dosages were calculated assuming the focus was at the surface of the sample in the middle of the vertical distance that was traveled.....	65
Table 8 Dosages for grown glass threshold maps in <i>Jscm2</i> . The dosages were calculated assuming the focus was at the surface of the sample in the middle of the vertical distance that was traveled.	67
Table 9 Dosages for nucleated glass threshold mapping in <i>Jscm2</i> . The dosages were calculated assuming the focus was at the surface of the sample in the middle of the vertical distance that was traveled.	68

LIST OF ACRONYMS

AS	Axially Symmetric
B	Base
ChG	Chalcogenide Glass
CW	Continuous Wave
DSC	Differential Scanning Calorimeter
EDS	Electron Dispersion X-Ray Spectroscopy
FEM	Finite Element Model
FIR	Far-Infrared
G	Grown Sample
HAZ	Heat Affected Zones
I	Rate of Nucleation
IR	Infrared
N	Nucleated
NIR	Near-Infrared
MIR	Mid-Infrared
RR	Repetition Rate
TEM	Transmission Electron Microscopy
T _g	Glass Transition Temperature
T _x	Crystallization Temperature
U	Rate of Crystallization

1 INTRODUCTION

A chalcogenide glass is a glass that contains at least one chalcogen (group 16) element, including Se, S, and Te. Oxygen and Polonium are not considered in this definition, since oxide glasses are already their own class, and Polonium is not normally used in glass. ChG glasses tend to have semi-conductor like properties, and have distinct band gap regions. They also are highly transparent in the infrared (IR) region of the electromagnetic spectrum. Depending on the composition of the glass, they can be transparent in some combination of the near-IR (NIR), mid-IR (MIR), and far-IR (FIR). [1]

ChG glasses tend to have lower bond strengths between the constituent atoms than traditional silicate glasses [2,3]. This leads to various common properties of this type of glass, including low melting temperatures [1,4], and photo-sensitivity [1-9].

1.1 Chalcogenides – Use As Optical Materials

Chalcogenide glasses (ChGs) have many different optical applications. ChG glasses have transparency windows in the IR region for a variety of glass compositions. The sulfides, selenides and tellurides possess much longer wavelength transmissions than glasses based on oxygen and silica [1,10,11]. Applications of ChGs include infrared lenses [1], waveguides [2,5-7,10], fibers [1,6], films [1], and gratings [2,6,7,12].

1.2 Chalcogenide Based Glasses and Glass Ceramics

Glass ceramics are glasses with sub-micron crystals throughout the glass matrix that have been grown in a controlled manner [11,13]. The glass ceramic can have improved

thermal and mechanical properties over the base glass, while still maintaining a possibility for loss cost mass production of optics for infrared applications [12,13]. The process of conversion, as discussed later is most commonly accomplished via a thermal heat treatment process, which relies on knowledge of the nucleation and growth behavior of the glass, which differs for each glass composition. Glass ceramics tend to exhibit an intermediate set of properties, usually between that of the glass and the precipitated crystal, which then can be used to increase the glass transition temperature of the original glass as seen by Mecholosky Jun et all [14]. Unfortunately the transmission at the lower wavelengths can also decrease with increasing scattering from crystals that grow too large or with a change in the band gap between the original glass and the ceramic [14]. One of the main issues with the development of glass ceramics is developing both the material and the conditions necessary to be able to control the size and distribution of nano-crystals in the glass matrix in order to maintain high transparency for the wavelengths needed [13].

Creating glass ceramics is traditionally done by heat treating a glass in a furnace [15]. Crystallization can occur when a glass is heated for a period of time, which depends on how close one is to the crystallization temperature, T_x , of the glass [16]. Typically, isothermal heating at an arbitrary temperature above the T_x results in spontaneous, uncontrolled crystal growth where the rate of nucleation (I) and subsequent rate of crystal growth (U) occurs first at the surface, and then within the volume of the material. This results in crystals with different properties, namely: different crystal phases, including differences in composition and therefore refractive index; size, which effects scattering; and the distribution of these crystals throughout the bulk glass matrix. The controlled

growth of uniform nano-crystals can be performed through specified heat treatments, which are defined by the nucleation and growth curve of the glass. Figure 1 shows an IU curve, which is representative of the nucleation and growth rates of a crystalline species in a glass [17,18].

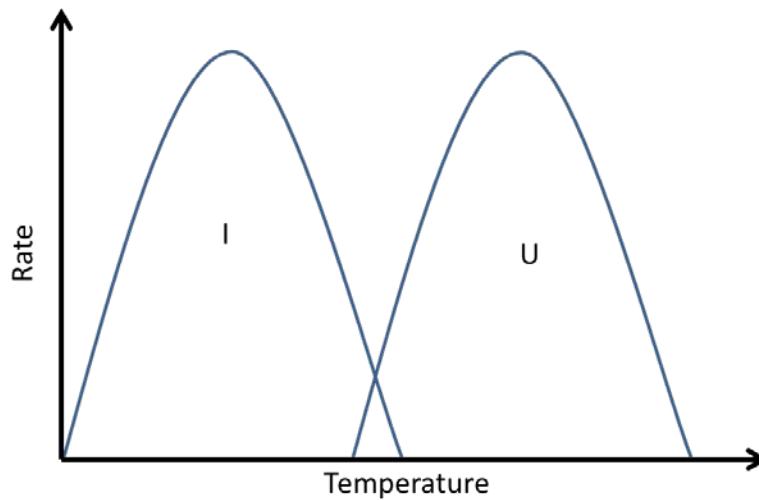


Figure 1 The representative rates of nucleation and crystallization are plotted against temperature, where I is the nucleation curve and U is the growth curve.

In a perfect material, which is suitable for ideal nucleation and growth of mono-sized crystals, the I and U curves would not overlap so that one is able to only nucleate, or only grow at the maximum rate. Unfortunately with real materials these two curves usually overlap to some extent so that the temperature chosen for a nucleation or growth step must be carefully chosen so that only one mechanism dominates at any given time.

Additionally there are a finite number of quenched-in nuclei from the glass forming process in the sample before any heat treatment is performed [15]. If one heats the sample under the nucleation peak, below the temperature where crystallization occurs, then one can create crystal nuclei throughout the sample [15,17]. These nuclei are typically several atoms across, and there are a finite number of sites in the glass where they can occur. If

the sample is heated long enough, all of these sites should be nucleated. If this sample is then heated at a temperature under the crystallization curve, but far enough from a temperature that has significant nucleation, than these nuclei can grow into crystals without forming any new nuclei [15,18]. The duration of this heat treatment will affect the final size of the crystals that are formed. The crystallization will affect the material properties, with the extent dependent on the size of, and volume fraction of the crystals. Figure 2 shows a representative cartoon of this occurring, where V_g is the volume fraction of glass, V_x is the volume fraction of crystallization, and the addition of V_g and V_x is one. In the original base glass it is assumed that there are no nuclei, even though as stated earlier there will be nuclei from the glass formation process.

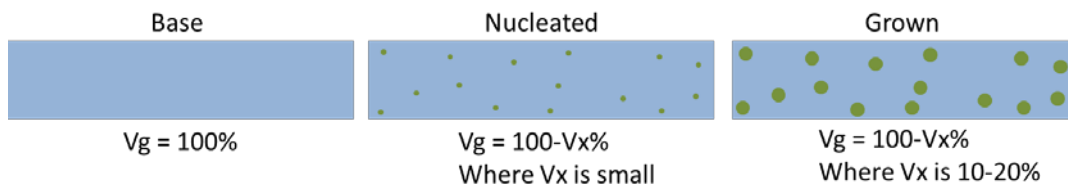


Figure 2 On the left is a base glass, which has a volume fraction of 100% of glass. The center picture shows a nucleated sample, which is base glass that has been heat treated at a temperature where nucleation can occur. The glass at this point has a volume fraction of glass, V_g , which is 100% minus a small amount due to the finite volume of the crystal nuclei, V_x . The right picture is of a grown sample, where a nucleated sample is subsequently subjected to a heat treatment where crystal growth occurs. The V_g is now 100% minus 10-20% V_x , as was used in this study.

In the nucleated sample nuclei have formed, and the sample is no longer completely glass since the nuclei each have a finite volume of a few atoms. The total volume of the nuclei though is small compared to the volume of the sample. In the grown sample the nuclei have grown to nano-crystals, where in our case the crystals are approximately 20-50nm in diameter, and take up a volume fraction of 10-20%. This volume fraction and

crystallite composition was confirmed with TEM and EDS for the samples used later in this study.

Since it is known that lasers can be used to heat materials, the ability for lasers to be able to nucleate and/or grow nano-crystals in a glass sample is probed in this study. As can be seen in figure 3, the aim of this work is to allow one to be able to go from base to grown glass in a spatially controlled manner and be able to predict what laser conditions would be needed to be able to grow nano-crystals in a specified manner.

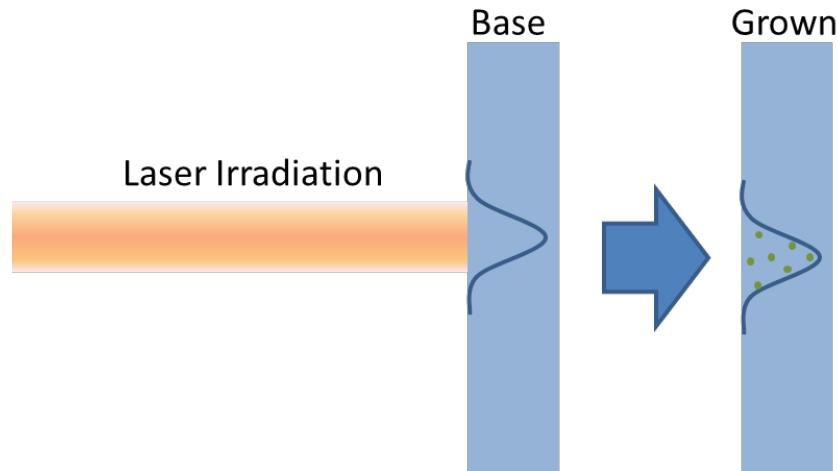


Figure 3 Laser irradiation should also be able to grow crystallites from a base or nucleated sample into a grown sample. The spatial extent and location of the growth would be controllable in this situation, which could lead to spatially modified material properties of a glass.

1.3 Photo-induced Processes

There are many properties that can be modified through exposure to light. Some of these changes are reversible, while others are permanent [5,6,9]. These changes include changes in band-gap (photo darkening and bleaching), refractive index, and density (volume expansion or densification) [2-9]. Needless to say, the way an induced material modification can impact an optical component's physical and optical properties is critically important for its use in an optical system. To date, a limited amount of

literature on photo-induced processes that relate to light-induced crystallization in infrared optical glass has been reported. These prior efforts are discussed below.

Photo-induced changes can occur from either broadband or narrow band light sources that are either coherent or incoherent. The type of source that is used can affect the changes that are observed in a given ChG material. Mercury arc and halogen lights were used in [19] to photo-amorphize Ge crystal, and showed it to be an athermal process. Normally though, the main type of light source used is a laser. Many different wavelengths have been used, with differing effects for the different wavelengths. Changes in the photodarkening effects were observed by Florea et al [11] in As_2S_3 with wavelengths of 568nm, 594nm, and 633nm used.

The main induced material properties that are studied include photo-darkening [20-23], photo-bleaching [22,23], refractive index changes [8,23], densification or expansion [4,5,7,9], ablation, and crystallization [20]. These effects result from changes in the glass network due to bond rearrangement and induced structural defects which are due to light interacting with lone pair electrons [20,22]. Some of the induced changes are reversible and can revert back to their original state after annealing at an elevated temperature [19,24]. Material property changes have been seen in bulk, film, and fiber samples. The irradiation conditions can change though between these forms due to differing thermal transport properties such as thermal conductivity [25] and thickness of material that is able to absorb the irradiation.

Laser irradiation can be used to make changes in the materials chemistry and/or phase. One application of laser induced melting is laser welding of either glass to glass or glass to another material such as silicon, where a bond is created from localized

modifications of chemistry in the joining process [26-28]. These investigations used fs laser pulses, and high kHz to MHz repetition rates (RR). Chalcogenide films have also been used in phase change devices where the chemistry is maintained, but the local irradiated region changes from amorphous to crystalline or vice versa. These tend to be used in non-volatile memory applications [13,25,29,30]. Here the material is switched between amorphous and crystalline phases by exposure to laser irradiation of different power levels [25,30]. These changes in phase can create changes in reflection [29] and electrical conductivity [30]. In this regime, typical attributes of interest include fast switching times, low laser power levels, and good material reversibility to the original start state.

The main properties of ChG glasses that are investigated in this study are the light-induced and thermally-induced modification of the glass, specifically ablation, expansion, and changes in Raman spectra. Since ChG glasses have electronic structures similar to semi-conductors there are two regimes that can be examined, the above bandgap and below bandgap irradiation conditions. For this paper reference to whether the light used is above or below the bandgap it will be in reference to the energy scale. The above bandgap energy regime can be approximated as surface heating, which assumes high absorption in the material being irradiated [31]. The below bandgap case can be approximated as a volumetric heat source since the low absorption in this case can allow heating below the surface. Incident light that is below the bandgap energy is more likely to cause changes due to an accumulated temperature increase or two photon absorption [8,9], since there is little linear absorption in this region. Though two photon absorption would tend to require higher intensities for the effects to be noticeable [6]. This thesis

examines the basic processes of laser-induced modification of ChGs using theoretical and experimental means with the ultimate goal of characterizing evidence of laser-induced modifications due to thermal or athermal processes.

2 RESEARCH OVERVIEW

Three materials were used in this study, a base, a nucleated, and a grown sample of a single composition of multi-component chalcogenide glass (ChG). These samples will be referred to as B (base), N (nucleated), and G (grown). The nucleated glass was heat treated in a furnace at a temperature that was high enough to nucleate, but below where significant crystallization should occur. The grown sample first underwent the same thermal treatment as the nucleated sample. It then had an added growth heat treatment at a temperature where crystallization occurs, and is above a temperature where additional nucleation can occur. This material is similar in composition to IRG-24 from Schott Glass, a Ge-As-Se glass. The material's physical and optical properties can be found in Appendix A. The material used in this study had a glass transition temperature (T_g) of 210°C and a T_x of 243°C . These were measured from the differential scanning calorimeter (DSC) curve in figure 4, where the inflection point on the left side of the dip around 200°C is the T_g of the glass, and the onset of the peak just past 240°C is the T_x of the glass.

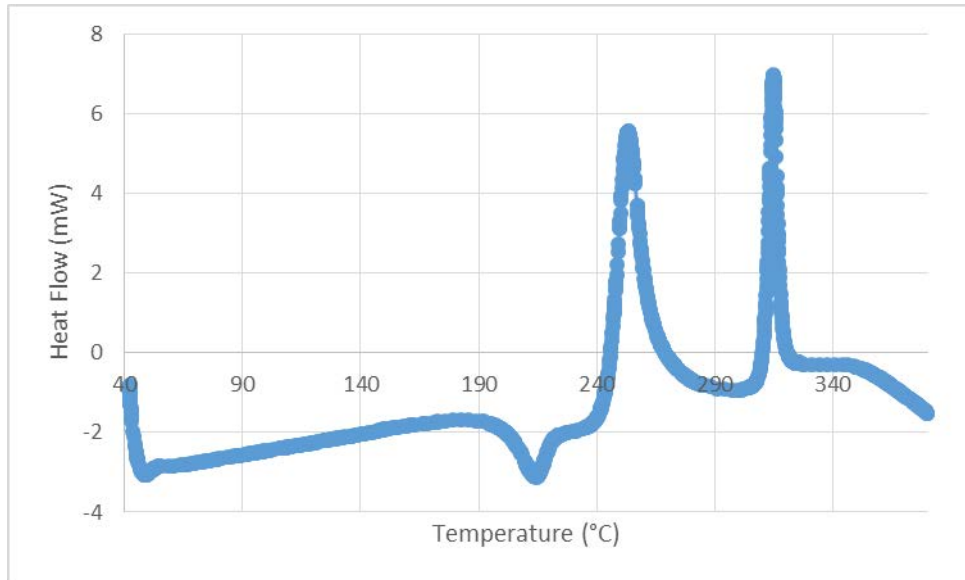


Figure 4 Shown is the heat flow measured from a DSC, where the inflection point on the left side of the dip around 200°C is the T_g of the glass, and the onset of the peak just past 240°C is the T_x of the glass

The glass used has a bandgap that is in the near-IR, and laser irradiations were performed with energies that were above and energies that were below this bandgap. In the above and below bandgap irradiation regimes the absorption from the laser is vastly different. In the sub-bandgap regime, the medium is highly transparent to the incident light and therefore linear absorption is small. While it has been shown that multi-photon absorption is possible in this regime [2] sub-bandgap irradiation typically relies on pulsed excitation with high pulse energies and/or RR to rely on heat accumulation within the sample. Conversely, laser-induced modification of a material using photons of energies above the optical bandgap, such as visible and near infrared light for the case of chalcogenides, one is in a regime where there is considerable absorption of the light by the medium. This limits the laser light's penetration depth to less than a micron as was seen by Stabl and Tichy in a GeAsS system [22]. In this case cw irradiation is usually sufficient to result in heat accumulation in approximately a surface heat source regime.

Additionally, as it has been discussed earlier, ChGs typically have low thermal conductivity and diffusivity. These property values slow the rate at which heat is deposited in the material and slow the rate at which it can be dissipated. As a reference, bandgap energies for ChGs are around 1.5-2 eV [23] for GeAsSe systems as compared to fused silica which is 9eV [32]. Additionally thermal conductivity values are about 0.25 W/mK for chalcogenides as compared to oxide glasses such as fused silica which is 1.2 W/mK [33].

2.1 Objectives and Goal

The overarching goal of this work is to be able to duplicate crystallization from a furnace with a laser. In order to determine the heat induced from laser exposure, simulations needed to be created. Several simulations were created in order to validate assumptions and calculations, which could then be checked against experimental observations. Ultimately knowing these things, we would like to predict and control dose, and therefore heating, to induce localized crystallization and phase change. These key project components are discussed briefly below.

2.2 Computational Tools

In this work Matlab and COMSOL Multiphysics computational tools were used. Matlab was used to solve for the temperature obtained from a laser beam that is incident on the surface, under certain geometries for the above bandgap case. The temperature could be solved for with an integral in general cases or as an analytical solution for the condition of looking at the center of the incident laser beam at the surface of the sample.

COMSOL Multiphysics was also used to solve for the temperature obtained from a laser beam that is incident on the surface of a sample. COMSOL though uses finite element method (FEM), and can account for more geometries than the model used for Matlab. Along with computational models, experiments were also performed.

2.3 Experimental Tools

Multiple tools were utilized in the experiments that were performed. Glass physical property tools such as the DSC discussed above were able to obtain several physical property measurements of the material. Two laser sources were used for irradiation, one below and one above the bandgap of the material. A 2 μ m Tm fiber laser operating in the ns pulse length and kHz RR regime was used for the below bandgap case and a 488nm laser was used for the above bandgap case. Exposures were controlled through LabView on an ESP300 which in turn controlled a Newport VP25XA stage and mechanical shutter. The effects from the different irradiation conditions were then determined with a white light interferometer (Zygo Corporation NewView, 6300), an optical microscope (Olympus BX51), and a near-infrared ($\lambda_{exc} = 785$ nm) Raman spectrometer (Bruker micro-Raman). The employment of these tools is discussed in Chapter 4.

2.4 Expected Outcomes

Following a discussion of the computational activities aimed at predicting the temperature distribution within a sample for a specific set of irradiation conditions, the experimental tests aimed at producing changes that are related to the temperature increase are described. Lastly, we conclude with a comparison and suggestions for further

improvements needed to predict the thermal distribution that is created for a set of irradiation conditions in a multi-component ChG sample.

3 COMPUTATIONAL TECHNIQUES

Since it is complex to be able to determine the temperature increase inside of sample, especially if one is using a focused beam of tens of microns to millimeters across, simulations were performed in order to determine the temperature distribution inside the material. Additionally simulations can be used to de-convolve changes induced thermally from those that are induced electronically. Different models are needed to determine the temperature increases for the above and below bandgap irradiation conditions that were used in this study. Figure 5 shows a representative absorption curve of a similar composition of the ones used. The two laser wavelengths used for heating were 488nm and 2 μ m.

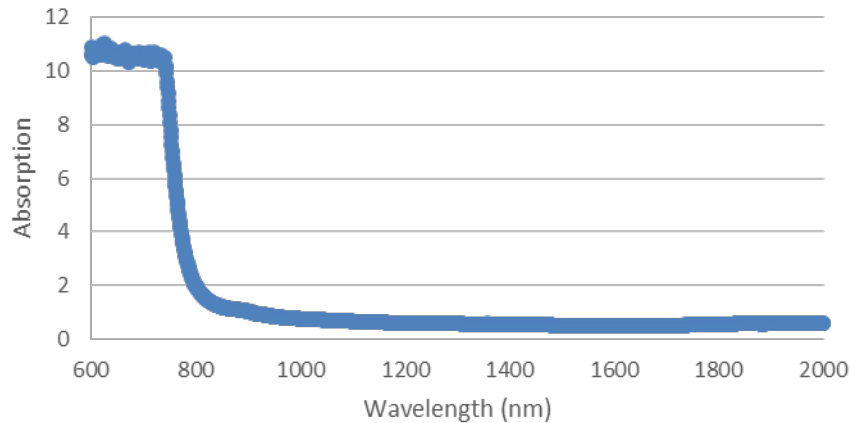


Figure 5 A representative UV-VIS absorption curve of a representative chalcogenide glass that is compositionally similar to the glasses used in this study

As one can see that 488nm is above the bandgap energy of the material, while the 2 μ m is below the bandgap energy of the material. The simulations used for the above band gap energies, for both finite and infinite boundary approximations, were performed with continuous wave (CW) incident light, while the simulations performed for the below bandgap light used pulsed laser light.

The computational programs used in this study to solve for the temperature increase in samples exposed to various laser irradiation conditions were Matlab and COMSOL Multiphysics. The two main models that were used were a semi-infinite boundary approximation model and a finite boundary model. The different models each have their own advantages and disadvantages, and were subsequently compared to see under what different assumptions could be considered valid.

The material property inputs for these simulations were a combination of measured property data for the materials used, and data from a commercial glass that is compositionally similar to the glass used in subsequent experiments. For some of the simulations all of the material properties were from the commercial equivalent, and for others the properties were representative of multi-component ChG as can be seen in table 1.

Table 1 Glass properties that were used in the various simulations, and where these values came from. See appendix A for the IRG-24 data sheet.

Experiments	Above Bandgap Energy	Below Bandgap Energy
Reflection Coefficient, R	0.27	0.27
Absorption Coefficient, α	Infinite (488nm)	1 cm ⁻¹ (2 μ)
Heat Capacity, Cp	0.37 $\frac{J}{gK}$	0.37 $\frac{J}{gK}$
Density, ρ	4.47 $\frac{g}{cm^3}$	4.47 $\frac{g}{cm^3}$
Thermal conductivity, k	0.19 $\frac{W}{mK}$	0.19 $\frac{W}{mK}$
source	IRG-24 Values + absorption approximation	IRG-24 Values

3.1 Semi-infinite Material Approximation

For the semi-infinite material simulations calculations were performed with formulations done by Hache et al [34]. The Finite models were produced in COMSOL, and followed the geometries used in subsequent experiments.

The semi-infinite material approximation used was based on work done by Hache et al [34]. The equations for various heat sources in a 2D-axially symmetric (AS) slab that has a surface heating source were derived in this work, and the heat equation for a Gaussian surface heat source is shown below in equation 1. This approximation is based on the geometry of the sample used. The geometry used employs the use of a 2D-AS slab where the model assumes that the material being heated extends to infinity in three directions, and has a finite edge that is incident to the laser beam. The model also assumes that this finite boundary is exposed to air. Additionally the model assumes that the incident laser beam has an intensity profile that is a perfect Gaussian operating in the CW regime, which is a valid assumption for the laser that was used. The surface heating used approximates the above bandgap energy regime.

For this approximation the boundary conditions for heat flow are as follows. First of all it is assumed that all irradiation is absorbed at the surface of the test sample described above, which leads to a surface-heating regime. It is also assumed that no heat is transferred from the edges of the material that extend to infinity, and heat transferred from the incident surface to the air is negligible. The geometry is seen in figure 6.

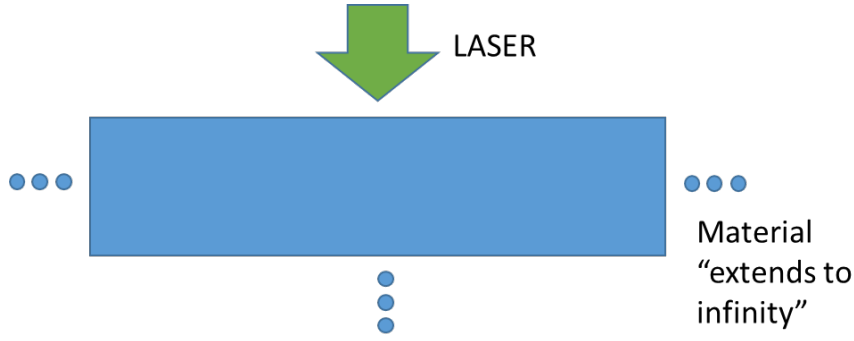


Figure 6 For the semi-infinite boundary approximation, the material “extends to infinity” in all directions except for the surface incident to the laser irradiation. This leads to no heat transfer at the boundaries that extend to infinity, and a negligible amount that leaves the incident surface.

From this approximation, one is able to solve for the heat distribution for all time by solving equation 1 as shown below where I_0 is the peak intensity of the laser (W/m^2), κ is

$$T(\rho, z, t) = \frac{wI_0}{2\kappa\sqrt{2\pi}} \int_0^{t_w} e^{-\frac{z(\rho/w)^2}{1+\tau} - \frac{z^2}{w^2\tau}} \frac{1}{\tau^{\frac{1}{2}}(1+\tau)} d\tau \quad (1)$$

the thermal conductivity ($\frac{\text{W}}{\text{mK}}$), D is the thermal diffusivity ($\frac{\text{s}}{\text{gm}}$), $t_w = \frac{z^2}{4D}$, ρ is the radial coordinate (m), w is the beam waist (m), and P is the incident laser power (W). This equation can then be simplified if one is interested in obtaining the maximum temperature that is seen by the sample, which is given below in equation 2.

$$T_{max} = \frac{P}{\kappa w \sqrt{2\pi}} \quad (2)$$

For these simulations Matlab was used to solve the integration of equation 1 with the adaptive Simpson quadrature function. The integration was used to be able to determine the radial distribution of heat at the surface of the sample at long times, or to see the rise time of the temperature at a single location on the sample. Equation 2 was solved for when only the maximum temperature obtained was needed.

3.2 Finite Boundary Model

The finite boundary models that were used were implemented in COMSOL Multiphysics. These simulations were performed in order to more closely match the geometries of the sample and beam sizes that were subsequently used in laboratory experiments, especially for the non-focused experiments which had beam sizes that were within an order of magnitude of the sample size. This violates the assumption of a semi-infinite material. Simulations were done with both 3D and 2D axially symmetric models, and were based on an available COMSOL model “Laser Heating - A Self Guided Tutorial” [35]. This model uses a stationary incident laser as a heat source that is implemented through the use of a heat transfer model as a surface or volumetric heat source with fixed geometry. The heat transfer equation used in the software is shown in equation 3. Volumetric heat sources were representative of below bandgap irradiances, and surface heat sources were representative of above bandgap irradiances.

$$\rho C_p \frac{dT}{dt} + \rho C_p u \cdot \nabla T = \nabla \cdot (k \nabla T) + Q \quad (3)[35]$$

For our simulations, this heat source could be either a CW source or a pulsed source. It was again assumed that the incident beam had a perfectly Gaussian intensity profile in the radial direction and is centered on the sample. The first order output mode for the fiber laser used in the below band gap experiments is actually a Bessel function, but is approximately Gaussian in the lowest order below the first zero of the Bessel function. The laser system that was used in subsequent experiments did not show signs of higher order mode content, so the approximation is valid for the conditions that were used. For these models finite edges were used with the boundary condition of convective heat flux as can be seen in figure 7.

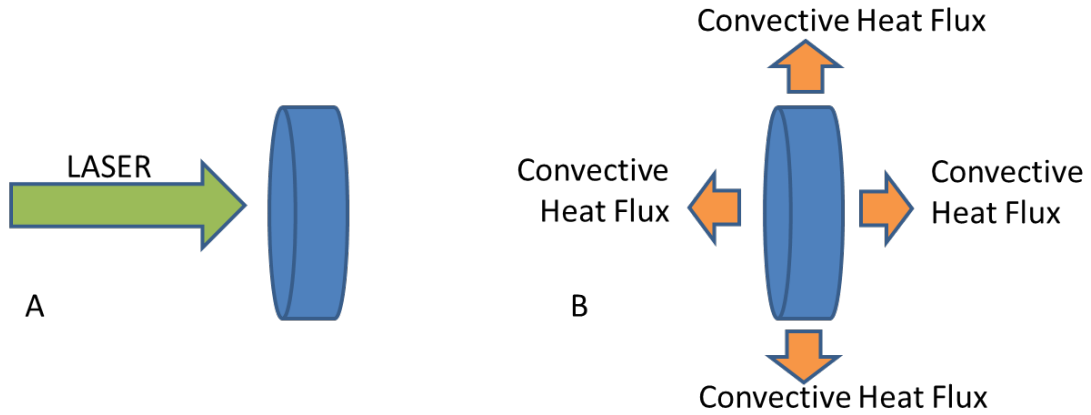


Figure 7 (a) Geometry used to describe the finite boundary condition as the laser beam hits the first planar input face of the glass surface, and (b) illustration of convective heat flux is able to leave the sample in all directions.

The main parameter that governs this is h , the heat transfer coefficient. In order to determine how this parameter would affect the solution, simulations were done with a varying h , and a difference of just under a degree in the maximum temperature for 100 pulses was seen as shown in figure 8. From this it was concluded that this parameter did not have a significant effect on the final solution when it had values between $10 \frac{W}{m^2K}$ and $100 \frac{W}{m^2K}$, and this parameter was set to $50 \frac{W}{m^2K}$ for subsequent simulations.

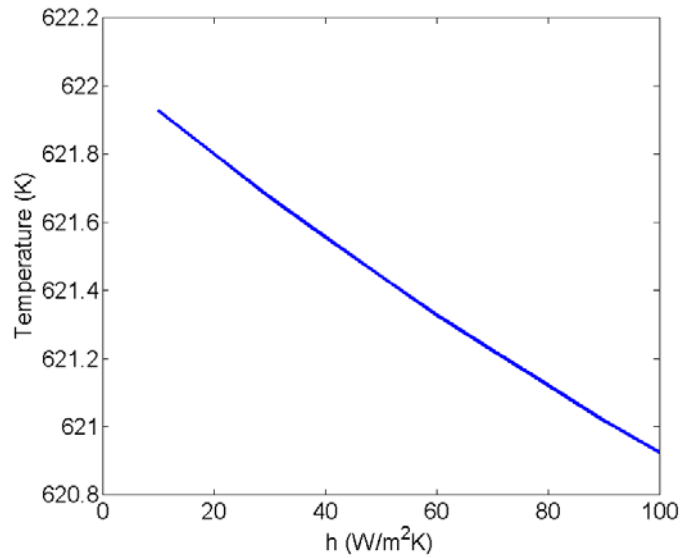


Figure 8 The maximum temperature obtained for simulations of 100 pulses of 2 μ m light was plotted against the heat transfer coefficient. There is only a small variation in the maximum temperature reached across this range.

3.3 Pulsed Laser Experiments

Simulations for below band gap energies were also solved for finite geometries; however, these simulations employed pulsed laser irradiation. The use of pulsed laser heat deposition into the sample was necessary in order to allow enough heat to be accumulated over multiple pulses, while using an incident power that was obtainable by the laser system used. Heat accumulation is able to build up in these materials due to their thermal properties, which cause there to be a slow decay of temperature between pulses so that the temperature is not able to go back to its initial state before the next pulse hits the sample [36] as seen in figure 9. This heat accumulation and the heat affected zone, HAZ, can be affected by both the pulse length and RR. It is well known [37] that fs pulses have smaller HAZ than ns pulses. Also it has been demonstrated that higher RR also have a larger HAZ [38].

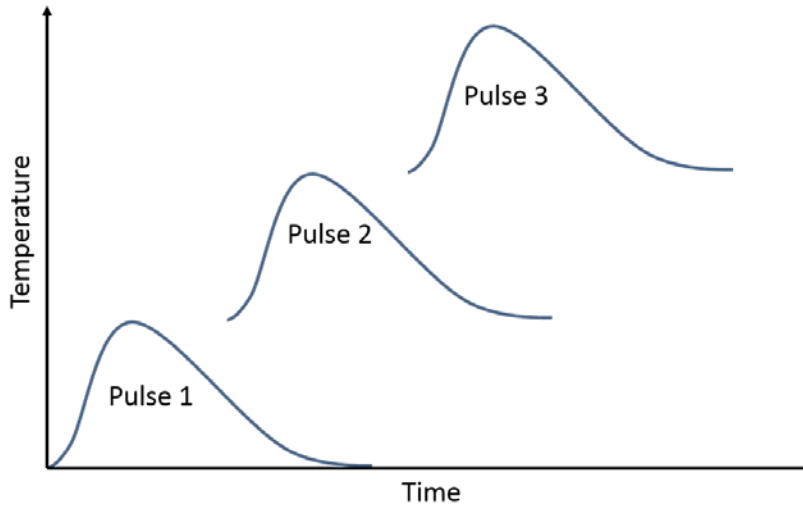


Figure 9 A schematic illustrating the temperature increase from individual laser pulses are plotted offset from each other. It can be seen that a temperature rise can start to occur for later pulses before the heat from previous pulses is able to dissipate completely if there is not enough time for the temperature to decay back to its original position. This leads to heat accumulation in the sample over many pulses.

The two time regimes that were used in the finite boundary simulations were CW and pulsed. For the CW case 2D-AS and 3D simulations were used. The 3D simulations were performed for geometries of samples or locations of the incident laser that were not axially symmetric. The 2D-AS models were used when possible since they required less mesh points and therefore need less computational resources and time to be able to generate a solution. The CW simulations were solved until a steady state was reached, while the pulsed simulations were solved for a specified number of pulses. Again the heat distribution at a given time on the surface, and the temporal rise of temperature at different locations were solved for.

For the pulsed regime 2D-axially symmetric and 3D models were created. In order to simulate the pulses, one needs to be able to have the solver operate on two different timescales, the duration of the pulse (20 ns) and the time between the pulses (0.05-1 ms). This was done by creating a time range and time-step between solver iterations for pulses

and the time between pulses. These were then concatenated together as input into the solver times of the time-domain solver of COMSOL. The time steps used were the length of the interval divided by a certain value, which will be referred to as the pulse divider. A larger pulse divider is indicative of a faster sampling rate of the heating equation with respect to time. The dependence of the solution on this value was then investigated to insure minimal error in the computation. Figure 10 pictorially shows how different time-steps within a single pulse can affect the accuracy of reconstruction of an input pulse where the vertical lines are the times where the solver is told to solve. The solver is active at times spaced by the FWHM of the pulse divided by the pulse divider or one over the RR divided by the pulse divider, depending on whether one is solving during a pulse, or between pulses respectively.

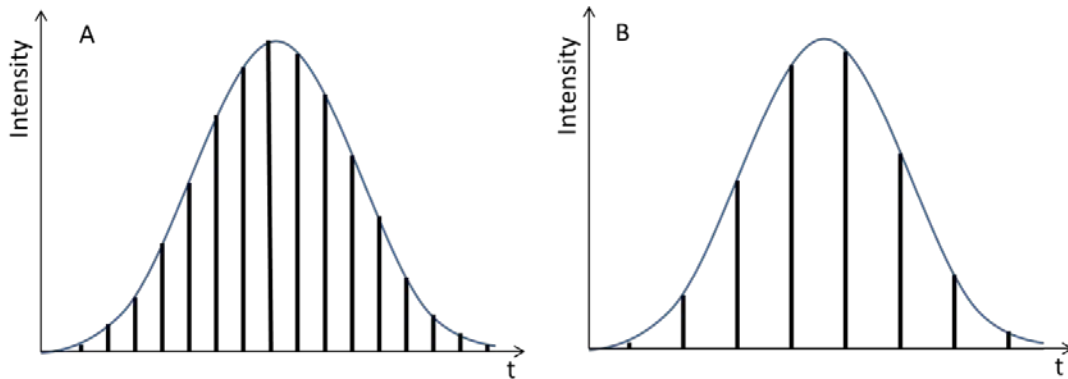


Figure 10 Sampling rates for a larger value for the pulse divider (A), and a smaller pulse divider (B). The time between sampling is defined as the pulse FWHM divided by a certain value which is defined as the pulse divider. As can be seen the larger the pulse divider, the closer the sampled function is to the actual input function.

The effect on the temperature from the time steps was then investigated. As can be seen in figure 11, the effect on the maximum temperature for 1 and 2 pulses was highly dependent on the time steps used. The maximum temperature appears to converge onto a

single value as the pulse divider is increased. The spikes that occur in the data are from computational inaccuracies that lead to differing solutions. For these simulations, a low relative tolerance of .01 was used by the solver.

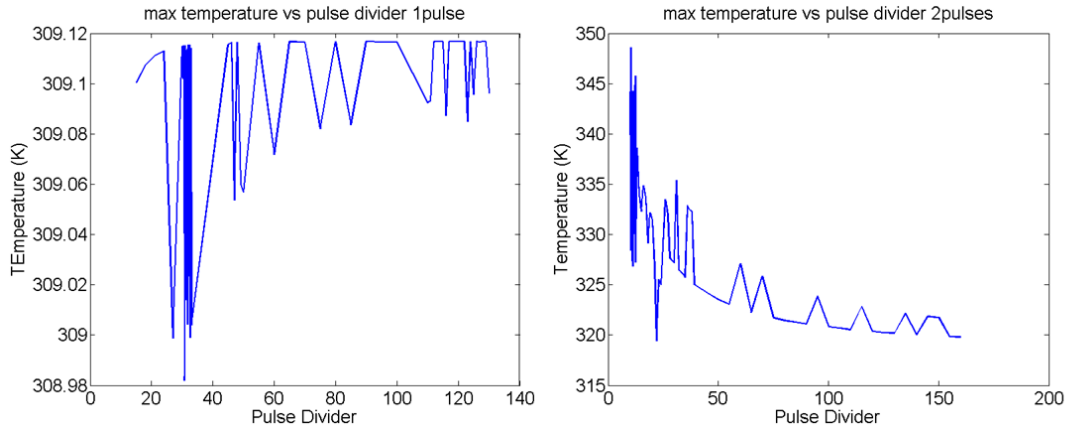


Figure 11 The maximum attained temperatures for different values of the pulse divider are plotted above for one pulse on the left, and two pulses on the right. As can be seen there is a large dependence of the maximum attained temperature on the pulse divider.

When the tolerance was increased to $1 \cdot 10^{-3}$, $1 \cdot 10^{-6}$ and $1 \cdot 10^{-9}$ the time dependence of the time step divider was calculated for 20 pulses as seen in figure 12. The change in the solution is seen to be much less for an increase in tolerance, and from this investigation into the uncertainty in the maximum obtained temperature in a sample from the finite sampling rate it is estimated to be around 10K for the $1 \cdot 10^{-3}$ case (figure 12 D), 3K for the $1 \cdot 10^{-6}$ case (figure 12 B), and 2K for the $1 \cdot 10^{-9}$ case (figure 12 A). The maximum temperature reached with a tolerance of $1 \cdot 10^{-9}$ was then solved for with 200 pulses (figure 12 C). This found an uncertainty of around 6K for pulse dividers below 12. This implies that the pulse divider has much less of an effect than the relative tolerance in the inherent uncertainty that is associated with the computations.

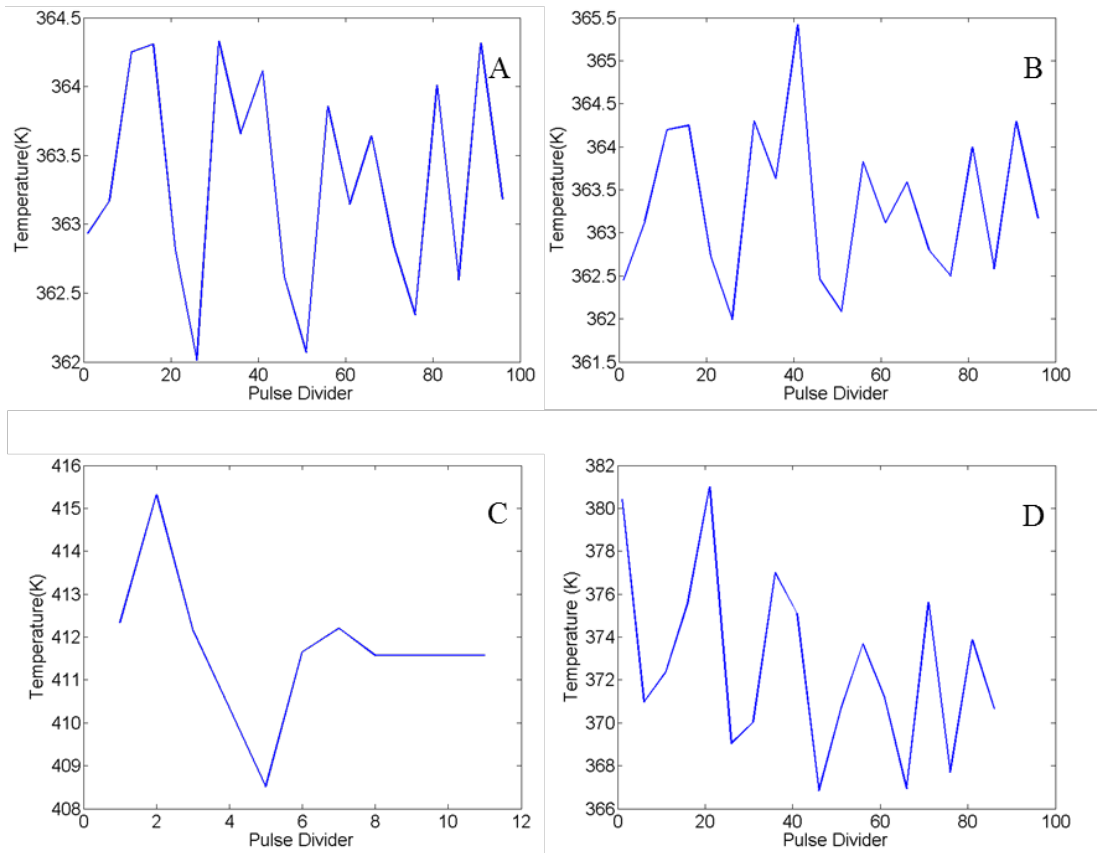


Figure 12 The maximum attained temperature is plotted against the pulse divider for different tolerances. (A) depicts a relative tolerance of $1E-9$ for 20 pulses, (B) depicts a relative tolerance of $1E-6$ for 20 pulses, (C) depicts a relative tolerance of $1E-9$ for 200 pulses, and (D) depicts a relative tolerance of $1E-3$ for 20 pulses. As can be seen, there is much less dependence of the maximum temperature on the pulse divider. There is through an associated uncertainty in the calculation that can be observed.

3.4 Comparison of Models

In an effort to evaluate the benefits and limitations of each of the models used, a comparison was made to assess capabilities and limitations in the resulting calculations. Specifically, the finite boundary and semi-infinite media approximation for CW irradiation were compared to see where the approximation of a semi-infinite medium either accurately represented the maximum temperature of the model, or began to break down. The continuous wave finite and infinite boundary models were looked into for

different beam widths while holding the other parameters of the simulations the same. This was done in order to determine when the infinite material approximation was valid, since this calculation is less computationally intensive and does not require specialized software, which would be preferable in certain situations. For this investigation the beam width of the incident laser irradiation was varied and the subsequent maximum temperature of the sample (T_{max}) was solved for. The following figure 13 [39] shows the percent difference in the maximum temperature between the two models as a function of the laser beam diameter divided by the diameter of the sample.

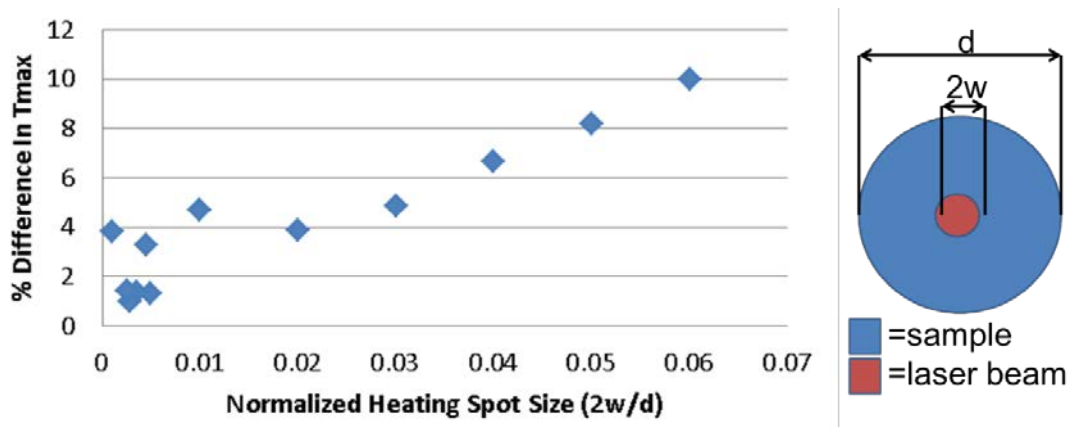


Figure 13 The percent difference in maximum temperature reached between the semi-infinite and infinite boundary models is plotted against a normalized heating spot size that is defined as two times the beam waist divided by the diameter of the sample. There is a clear trend of deviation that can be seen as the size of the laser beam is increased since the infinite boundary approximation becomes invalid. At small beam sizes the finite boundary model is not able to properly solve the equations due to the finite size of the meshing used in the simulation. From [39].

From this plot it can be seen that there is a clear trend of divergence between the two samples as the diameter of the laser beam is increased. At low beam diameters there tends to be a bit of deviation from this trend. This is most likely due to the beam diameter being on the order of the mesh size that was used, and therefore computational errors could be

occurring. The finite mesh size was due to the limited computational resources that were available at the time.

From this plot it has been determined that for a beam diameter which is less than 2% of the sample diameter, the semi-infinite approximation appears to be reasonably valid. For the 10mm diameter samples that were used, this would correspond to a beam diameter of 200 μ m. For some of the experimental conditions that were subsequently performed, beam diameters on the order of a couple of millimeters were used, so finite boundary simulations were used for subsequent simulations.

3.5 Summary

It has been shown that two types of computational models can be used to predict the induced temperature changes on chalcogenide glass from incident laser irradiation. Multiple models have been created, including a semi-infinite CW model, a finite boundary CW model, and a finite boundary pulsed model in order to account for various irradiation and geometrical conditions that were to be used in experiments. In conditions where above bandgap irradiation was employed, the use of both finite and semi-infinite boundary conditions are valid if the incident laser beam waist is less than 200 μ m, otherwise the use of a finite boundary condition is needed. For the below bandgap irradiation, a pulsed regime is needed for heat accumulation to occur. The model used in this study also employed finite boundary conditions. Lastly the relative tolerances in the COMSOL model and the sampling rate of the input heat source was examined. It was found that variation of the sampling rate have minimal impact on the resulting uncertainty in the calculated data points as compared to changes in the relative tolerances.

Additionally, using a smaller tolerance value and lower sampling rate had a lower computation time than a higher tolerance value and a larger sampling rate.

4 EXPERIMENTAL VALIDATION OF COMPUTATIONAL MODELS

Experiments were performed with laser irradiation that had photon energies either above the bandgap energy or below the bandgap energy. Induced material property changes from laser irradiation were examined for our ChG samples under these two different exposure conditions. Thresholds for various changes including expansion and ablation were investigated in the below band-gap condition. The above bandgap irradiation was performed with a 488nm CW laser, while the below bandgap was performed with a 2 μ m, ns pulsed laser with pulse lengths of either 10 or 100ns for average powers between 26mW and 40mW for the focused experiments. This corresponds to operating in an energy regime spanning .026-.04mJ/pulse for a 1 kHz RR. Discussed in the subsequent sections are the experimental conditions used in the laser exposure experiments for both CW above bandgap exposures and pulsed sub-bandgap exposures. Following these discussions are the findings of experiments aimed at inducing a temperature rise in laser-heated samples and the resulting physical impact of the irradiation. Lastly, Chapter 5 compares these experimental findings to those calculated in the simulations.

4.1 Above Bandgap Energy

The above bandgap energy laser irradiation was performed with a 488nm laser operated in the CW regime. The goal of this experiment was to induce photo expansion as had been seen by Tanaka et all [9] in As₂S₃ glass. The samples for this set of experiments were held in a vertical orientation as seen in figure 14. The incident laser had a beam radius of 1.3mm, the beam expander had a focal length of about .5m, and the sample was

not located at the beam waist. The samples were irradiated at power levels of 450 and 500mW.

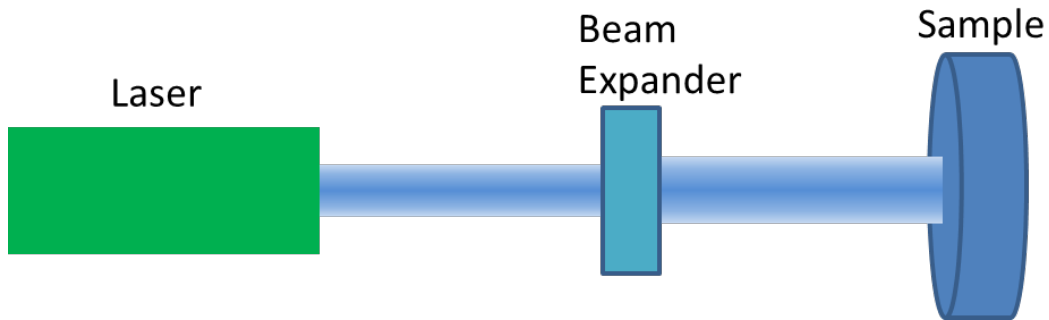


Figure 14 The laser setup that was used in the above bandgap exposures is shown. A 488nm laser was expanded and then hit the sample that was held in a vertical position.

4.2 Below Bandgap Energy Radiation

The below bandgap energy laser irradiation was performed with a 2 μm ns pulsed laser. The laser system used is shown in figure 15 and is discussed in [40]. The system is homebuilt and offers slight wavelength tuning, RR of 1-20kHz, possible CW operation, and pulse lengths of 7-100ns. For these experiments the samples were oriented horizontally as seen in figure 15. The sample was placed on a holder that was connected to a 3D stage (Newport VP25XA) which was able to be controlled through an ESP300 with LabView software.

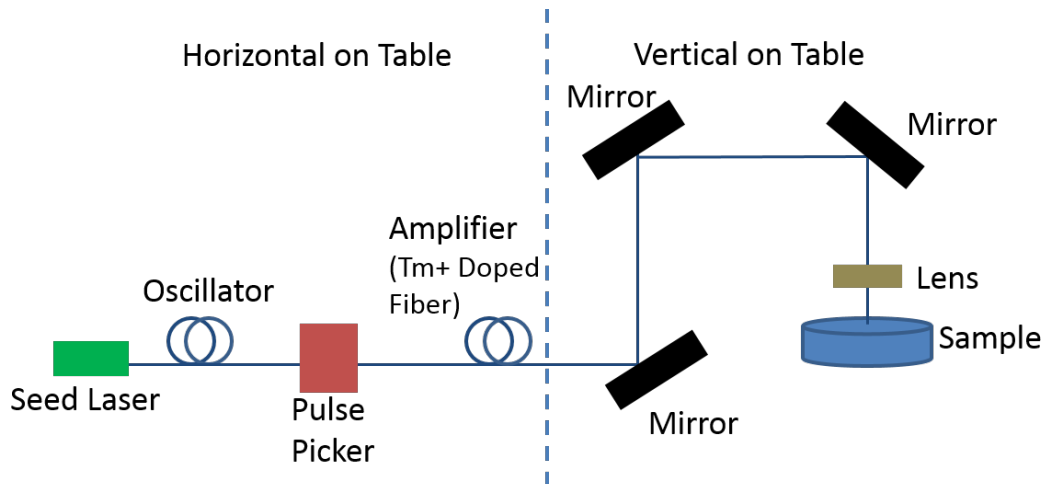


Figure 15 The laser setup that was used in the below bandgap exposures is shown. The $2\mu\text{m}$ laser starts with a seed laser in an oscillator. This then goes through a pulse picker to be able to have different repetition rates. This then goes into a thulium doped fiber and is amplified again. The output from this is brought vertically off of the table in order to be able to have a sample in a flat position, since this set-up is used for various other machining experiments.

Two different types of exposures, large area and focused exposures, were performed with a RR of 20kHz, and a pulse width of 20ns. The large area exposures were done by expanding the output from the laser so that the intensity of the beam was roughly even across an added aperture that was 8mm in diameter and was placed above the sample. 10mm diameter samples of each of the three materials discussed in the introduction were cut into four pieces and each of these four pieces received a different laser power, while maintaining the same exposure time of 5min. The samples were placed directly beneath the aperture, and were held at that location for the entire exposure. The powers used were measured below the aperture and were 0.2, 0.4, 0.8, and 0.95 W.

Next, experiments were done with focused laser beams in order to reach higher intensities on sample. Here, the assumption was that higher intensities would yield an increase in local heating, though care was taken to try to remain below the ablation threshold where damage would occur. For the first set of these experiments a beam waist

of approximately $7\mu\text{m}$ was used on the same three materials. The focus of the laser was located at the surface of the sample for the irradiations. In order to be able to have large enough areas to potentially be able to see material changes, arrays of individually exposed points were used as shown in figure 16. The arrays were 10×10 sets of points that were irradiated for 2 s at each point. Multiple of these arrays were done on each sample with different power conditions being applied to different arrays. The powers that were used were 0.159, 0.08, 0.032, 0.0045, and 0.00179 W.

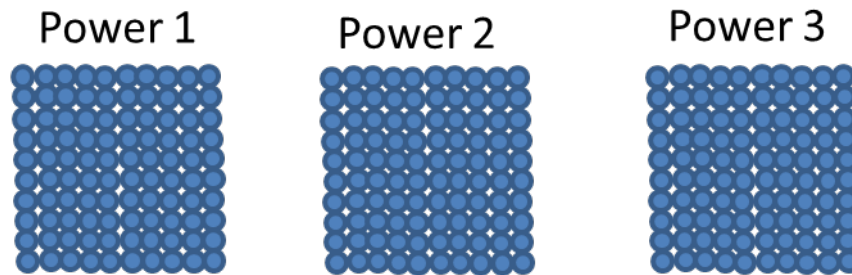


Figure 16 The arrays that were used in the focused experiments are shown where 10×10 individual spots were exposed for 2 s each. Multiple arrays were exposed near each other with a different incident power level applied to each array.

Several issues were noticed in these irradiation experiments. The first was making sure that the beam focus was actually on the surface. The second was making sure that the incident surface of the sample was actually perpendicular to the incident beam so that it would not deviate from the surface as the sample was translated while writing the arrays. Lastly there was question on non-uniformities in the samples that could lead to non-uniform interactions with the laser from either pits or scratches from the polishing and/or from a non-uniform distribution of the composition of the material. In order to try to correct for the first issue a different RR of 1 kHz was chosen. This was done in order to increase the pulse intensity so that a larger beam waist, and therefore working distance, could be used while maintaining the same average intensity from the laser. To attempt to

correct the second issue, slight corrections were made to the last portion of the beam path that was assumed to be vertical, and the amount of wedge in the samples was measured. The compositional part of the third issue could not be properly evaluated or corrected for in this study, though improvements in the material and the fabrication of samples are being worked on.

4.3 Threshold Mapping

Prior work by Petit et al [4] showed how the dose and intensity of laser irradiation could yield changes in either optical or optical and physical characteristics of bulk specimens. In these studies, an ablation threshold map was used to attempt to understand the irradiation conditions where transitions occur between these phenomena. These thresholds were largely found to relate strongly to average bond strength of the medium and its overall network structure. Threshold maps associated with the laser dose induced modification from the 2 μ m irradiation were created in the chalcogenide glasses in the present study. As has been shown in previous work [4], two dimensional spatial maps are normally made from an array with increasing power in one direction and exposure time in a second one. This allows one to be able to obtain an array of varying dosages, which is defined in equation 4.

$$dose = \frac{2P_{avg}}{RR * \pi w_0^2} * t_{exposure} \quad (4)$$

The threshold mapping for the three materials being investigated was performed with the same laser set-up that was used in section 4.2 (see figure 15). For this experiment the RR was decreased to 1 kHz in order to allow for a larger beam waist, and therefore longer working distance, while still maintaining the intensities previously used. Since there was

uncertainty in whether the focus was directly on the samples in previous experiments, the threshold was done slightly differently than normal. For this study the time of exposure and amount of incident power were varied as normal, but an added variation in height was added as can be seen in figure 17.

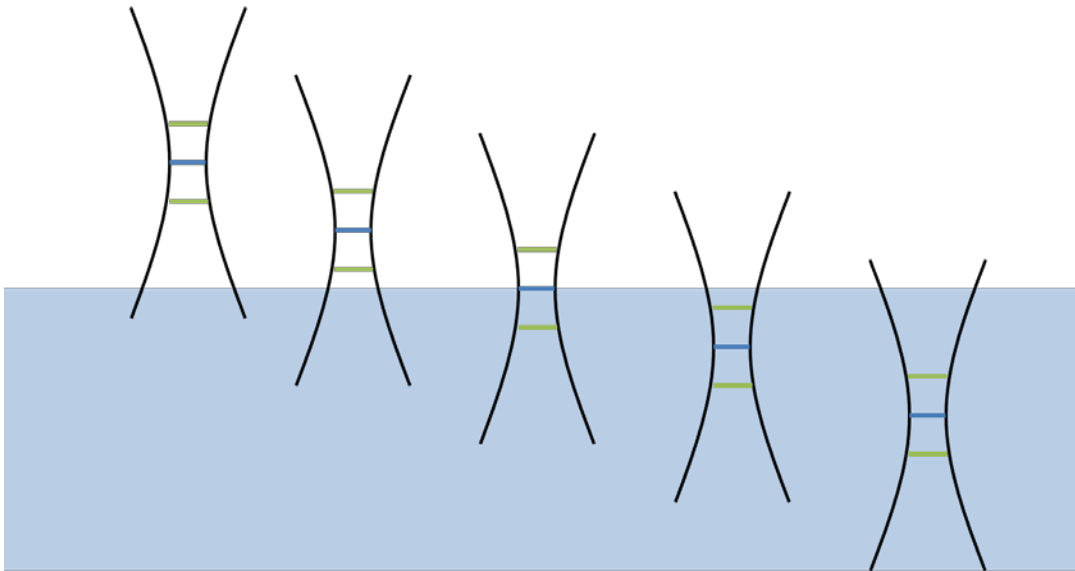


Figure 17 For the threshold experiments the laser focus was varied vertically. The horizontal blue line represents the beam waist, and the two green lines represent the Raleigh range of the beam.

The threshold map for the base glass is shown in figure 18. Each box represents a different duration of time, including 0.05, 0.5, 1, 10, and 20 s for this sample. The circles inside of these boxes represent the location of the laser for the different exposures. The vertical columns of circles shown in the figures 18-20 correspond to a single power level. The grayscale at the bottom gives a representation of the relative power levels that were used for each of the time sections where black is the highest power level and white is the lowest power level.

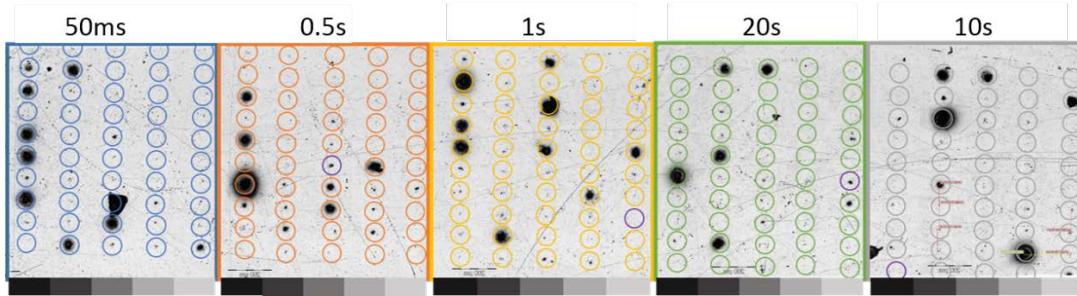


Figure 18 The threshold map for the base glass is shown. The vertical lines correspond to different power levels, while the horizontal lines correspond to different heights of the focus. The squares correspond to different timescales used. The purple circles correspond to locations where expansion was observed.

Table 2 The maximum and minimum dosages for the different exposure times overall and for the irradiated areas that saw damage is shown for the base glass. The dosages were calculated assuming the focus was at the surface of the sample in the middle of the vertical distance that was traveled.

Exposure Length (s)	Maximum Dose ($\frac{Js}{cm^2}$)	Minimum Dose ($\frac{Js}{cm^2}$)	Maximum Dose with Ablation Seen ($\frac{Js}{cm^2}$)	Minimum Dose with Ablation Seen ($\frac{Js}{cm^2}$)
0.05	0.302	0.196	0.302	0.196
0.5	2.743	1.820	2.743	2.215
1	5.474	3.682	5.474	4.254
10	54.261	36.196	51.404	36.196
20	109.731	72.811	109.054	86.845

The dosages that were used for the base, nucleated, and grown samples and the corresponding powers and dosages can be found in Appendix B, where the dosages were calculated assuming the focus was at the surface of the sample in the middle of the vertical distance that was traveled.. The maximum and minimum dosages for the different exposure times overall and for the irradiated areas that saw damage is shown above in table 2 and below in tables 3 and 4. The horizontal lines of circles refer to the vertical

position in the sample, where the focus is moved from below the surface of the sample at the top end of the picture, to above the surface of the sample at the bottom end of the picture. The sample was moved vertically in 50 μ m increments between these lines, and the focal point of the laser should have been on the surface within the range that was moved. The maps for the nucleated and grown are shown in figures 19 and 20, and the maximum and minimum dosages are shown in tables 3 and 4 respectively. The maps were set up the same as for the base, except for in the case of the grown where the time scales are stacked vertically instead of horizontally.

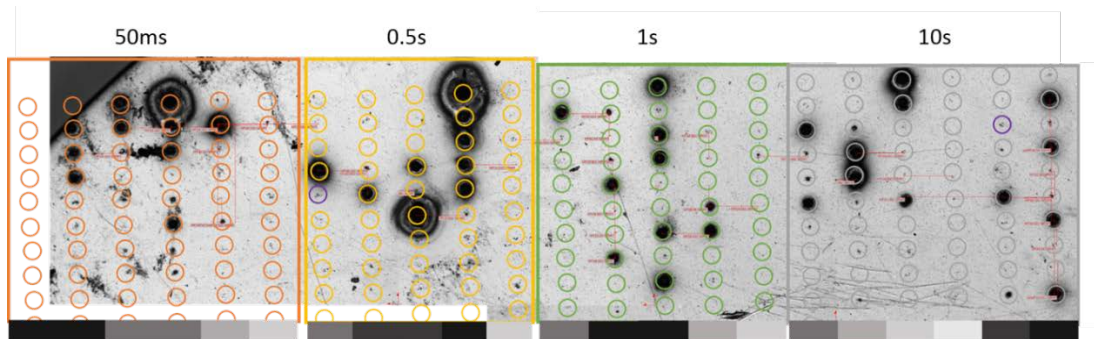


Figure 19 The threshold map for the nucleated glass is shown. The vertical lines correspond to different power levels, while the horizontal lines correspond to different heights of the focus. The squares correspond to different timescales used. The purple circles correspond to locations where expansion was observed.

Table 3 The maximum and minimum dosages for the different exposure times overall and for the irradiated areas that saw damage is shown for the nucleated glass. The

dosages were calculated assuming the focus was at the surface of the sample in the middle of the vertical distance that was traveled.

Exposure Length (s)	Maximum Dose ($\frac{Js}{cm^2}$)	Minimum Dose ($\frac{Js}{cm^2}$)	Maximum Dose with Ablation Seen ($\frac{Js}{cm^2}$)	Minimum Dose with Ablation Seen ($\frac{Js}{cm^2}$)
0.05	0.326	0.188	0.326	0.254
0.5	3.287	2.007	3.287	2.880
1	6.333	3.797	6.294	4.856
10	63.326	34.943	63.32584	43.593

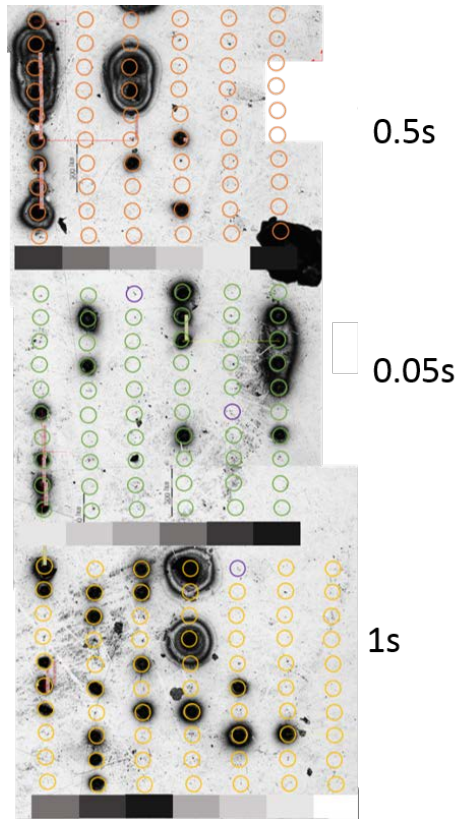


Figure 20 The threshold map for the grown glass is shown. The vertical lines correspond to different power levels, while the horizontal lines correspond to different heights of the focus. The squares correspond to different timescales used. The purple circles correspond to locations where expansion was observed.

Table 4 The maximum and minimum dosages for the different exposure times overall and for the irradiated areas that saw damage is shown for the grown glass The dosages were calculated assuming the focus was at the surface of the sample in the middle of the vertical distance that was traveled.

Exposure Length (s)	Maximum Dose $\left(\frac{Js}{cm^2}\right)$	Minimum Dose $\left(\frac{Js}{cm^2}\right)$	Maximum Dose with Ablation Seen $\left(\frac{Js}{cm^2}\right)$	Minimum Dose with Ablation Seen $\left(\frac{Js}{cm^2}\right)$
0.05	0.341	0.183	0.323	0.210
0.5	3.227	1.747	3.227	1.747
1	6.453	3.321	6.453	3.793

It can be seen that the ablation in the material does not appear to have a specific pattern that is followed, and there is no obvious sign of a height where that focus is at the surface of the sample.

4.4 Characterization of Material Property Changes

Laser induced modification across the varying irradiation regimes discussed above were shown to result in a variety of physical changes to the glass samples. These samples were evaluated pre- and post-irradiation to try to correlate material response with illumination conditions. The three main avenues used to determine material property changes were a white light interferometer (Zygo Corporation NewView, 6300), an optical microscope (Olympus BX51), and near-infrared ($\lambda_{exc} = 785 \text{ nm}$) Raman spectrometer (Bruker micro-Raman). The uses of the various characterization tools are summarized in table 5 below.

Table 5 Characterization tools used for each experiment and what information can be obtained from each of them.

	Above Bandgap	Below Bandgap Threshold Mapping	Below Bandgap Focused Exposures	Below Bandgap Wide Area Exposures	What Information Can Be Obtained
Micro-Raman				x	Bond-information
White Light Interferometer	x	x	x	x	Surface Deformation
Visible Microscope		x	x		Visible Surface Changes

For the threshold exposures below the bandgap there were many similarities in the surface changes that were observed on the different types of samples. In almost all of the exposures done in the threshold study where there was no ablation, there appeared to be small melt pools that were several microns to tens of microns in size. Examples of these pools can be seen in figure 21 on the right side. These melt pools occur for dosages across three orders of magnitude and tend to have several small pools clustered together with a fairly uniform distribution.

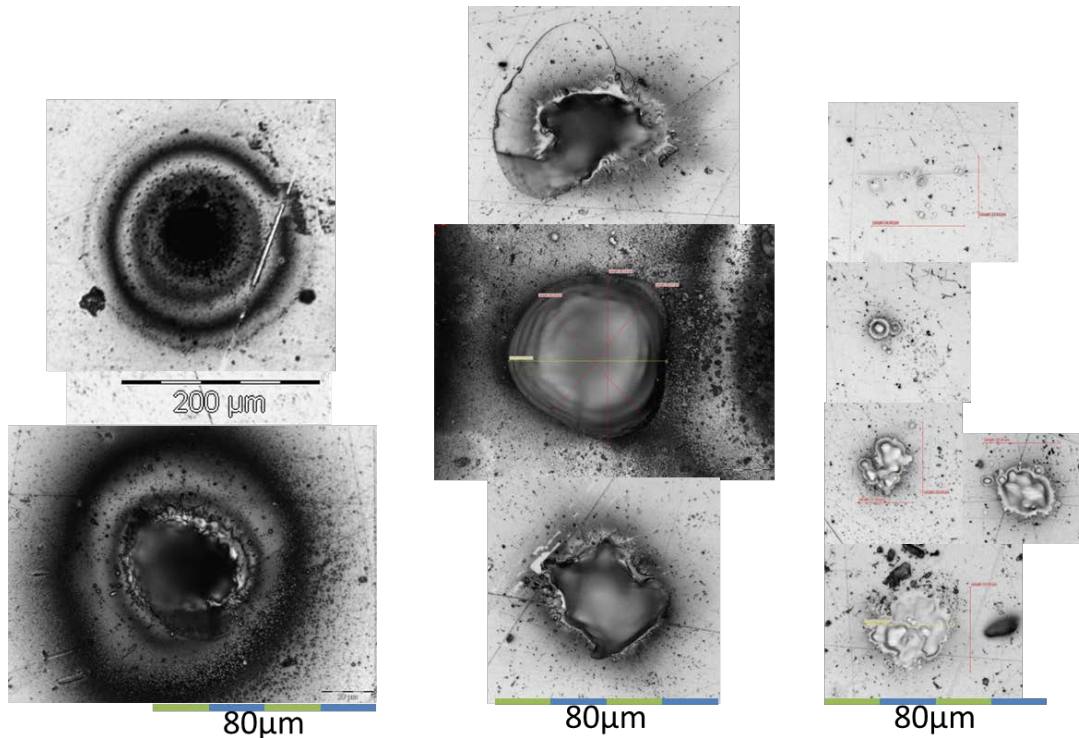


Figure 21 Various material changes can be seen from a visible microscope including ablation with one or more halos, thermal stress fractures, and small melt pools.

It is believed that the positioning stage and the laser are stable and therefore would not be shifting during the exposures and therefore create multiple melt sites. Also there is not a higher concentration in the center of an irradiation location with a decrease in concentration moving farther from the center that would indicate that it was an intensity based process. It could be possible that crystallization had occurred, and these growing crystallites could have a higher absorbance than the surrounding material and therefore melt preferentially. If this were occurring though, it would seem reasonable that there would then be a size distribution that followed the intensity distribution of the incident radiation.

As well as the melt pools, other visual changes were also observed. The easiest to see is ablation, which was generally also accompanied by crystallization. Most of the crystals

are fairly small, but some of them can be seen as shown in figure 22. The amount of crystallization that is seen around the ablation crater is seen to increase with an increase in diameter of the crater and creates an indicative “halo” around crater. Some of the craters have double halos. The formation of these could be attributed to complex heating and cooling conditions and can be seen on the left in figure 21.

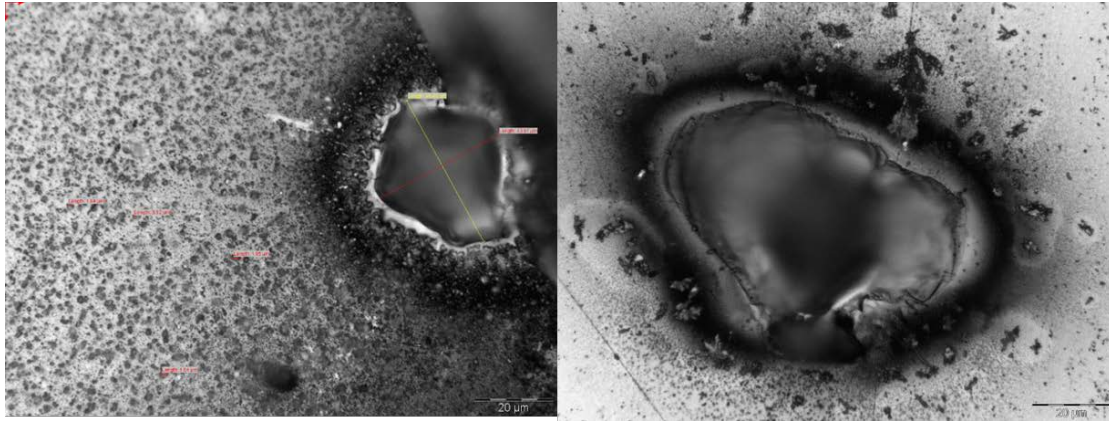


Figure 22 Crystallization was observed around various ablation craters. The bar in the micrographs is 20 microns.

There were also several other notable features from the irradiation, which can be seen in the center column of figure 21. At the top of the column one can see an example of a stress fracture that has a piece missing. The middle picture shows an area that has a distinctly ablated circular region, but does not have evidence of a crater rim. This was the only irradiation spot where this was observed. The bottom picture shows a hole that is halfway between a melt pool and an ablation crater where there is a splatter crater rim that is starting to form, but there is not yet a circular hole, or a significant halo.

From the white light interferometer it was seen that photo-expansion can occur with some of the irradiation conditions that were used. These instances are hard to observe, since they tend to be fairly small expansions and masking of surrounding ablation is necessary to be able to observe them. These can be seen in figures 23-25. These expansions were

found at varying dosages of between $2.33 \cdot 10^{-1}$ and $8.36 \cdot 10^1 \frac{Js}{cm^2}$. Most of the expansion sites had melt pools over part of the expanded area.

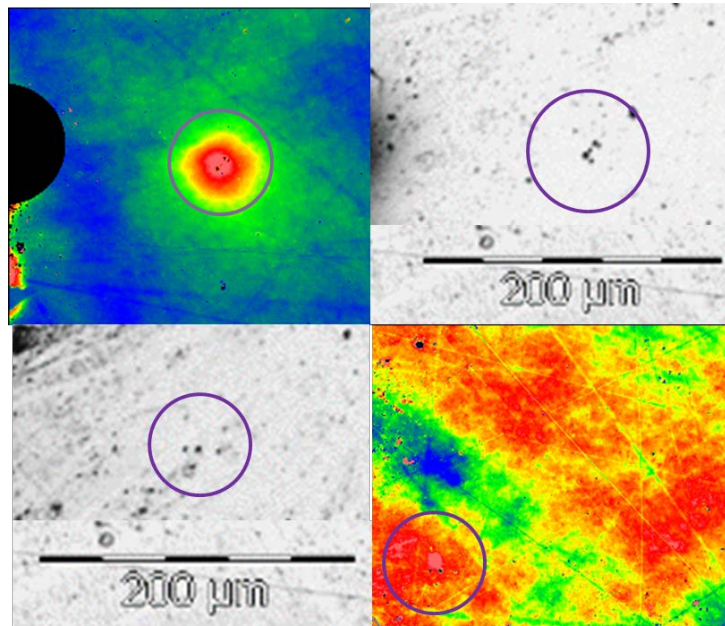


Figure 23 Visible and white light interferometer images are side by side for examples of expansion that was observed in the grown samples. The purple circles mark the area that was exposed.

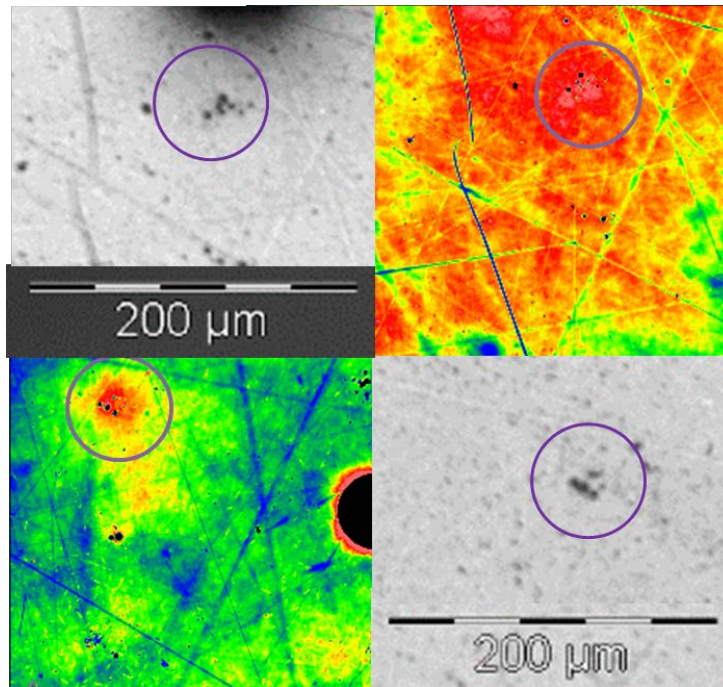


Figure 24 Visible and white light interferometer images are side by side for examples of expansion that was observed in the nucleated samples. The purple circles mark the area that was exposed.

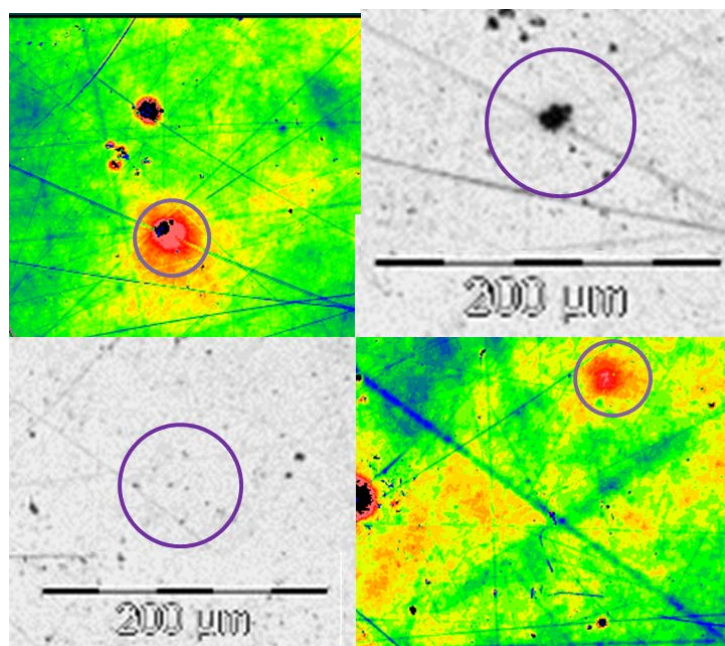


Figure 25 Visible and white light interferometer images are side by side for examples of expansion that was observed in the base samples. The purple circles mark the area that was exposed.

For the wide area, below bandgap exposures there were not any changes that could be seen by visual inspection. In order to detect changes, Raman spectroscopy was performed on the samples as seen in figure 26 since the exposed areas were large enough to probe with this technique. The excitation wavelength of 785 nm was chosen in order to prevent further material property changes from the measurement. The spectra was normalized by the total area under the signal data. Below in table 6 are six peaks that were tracked between the different irradiation conditions and what bonds they represent.

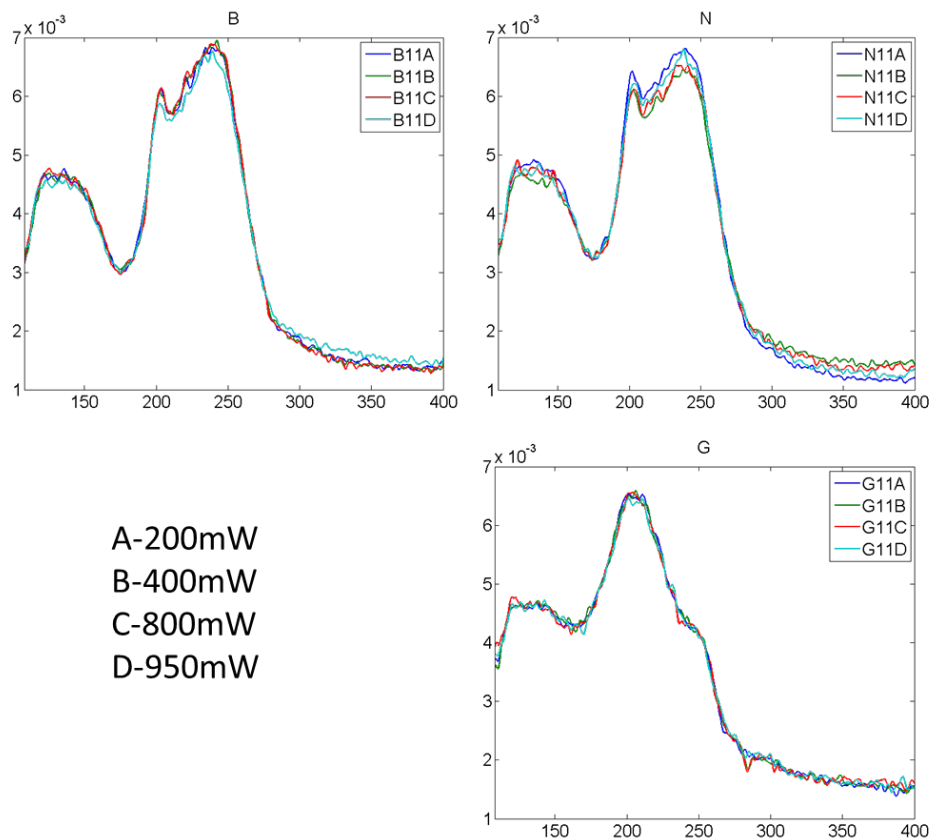


Figure 26 The Raman spectra for the wide area exposures is shown. The upper left is for base, the upper right is for nucleated, and the lower right is for the grown samples. The lines for A-D are representative of the different power levels the samples were exposed to, and their values are shown in the bottom left.

Table 6 Assignments to Raman peaks that were monitored for the normalized results.

Peak	Wavenumber (cm^{-1})	Mode	Source	Material
1	119	GeSe _{1/2} 4 F2 mode	[41]	GexPxSe1-2x
2	132	P4Se3 monomers (E mode)	[42]	GexPxSe1-2x
3	151	150	[43]	PbSe (crystal)
4	201	Ge-Se vibrations in [GeSe ₄] tetrahedrons	[44]	GexAsySe100-x-y
5	221	As-Se vibration band	[44]	GexAsySe100-x-y
6	244	GeSe _{4/2} symmetric stretching	[45]	Ge33Se67

There were slight changes in the intensities of the various peaks that were monitored from the normalized data. As can be seen in figure 27. In the graphs the blue trace is the base glass, green is the grown glass, and red is the nucleated glass. There were no clear trends though between the different irradiated power levels. The most significant change is not between the power levels, but between the sample types. As can be seen in figure 27 in peaks 1, 5, and 6, which corresponds to a GeSe_{1/2} 4 F2 mode, As-Se vibration band, and GeSe_{4/2} symmetric stretching respectively, tend to be lower on the grown sample than the base or nucleated. The small changes that occur could be representative of the small volume fraction of crystallites in the material.

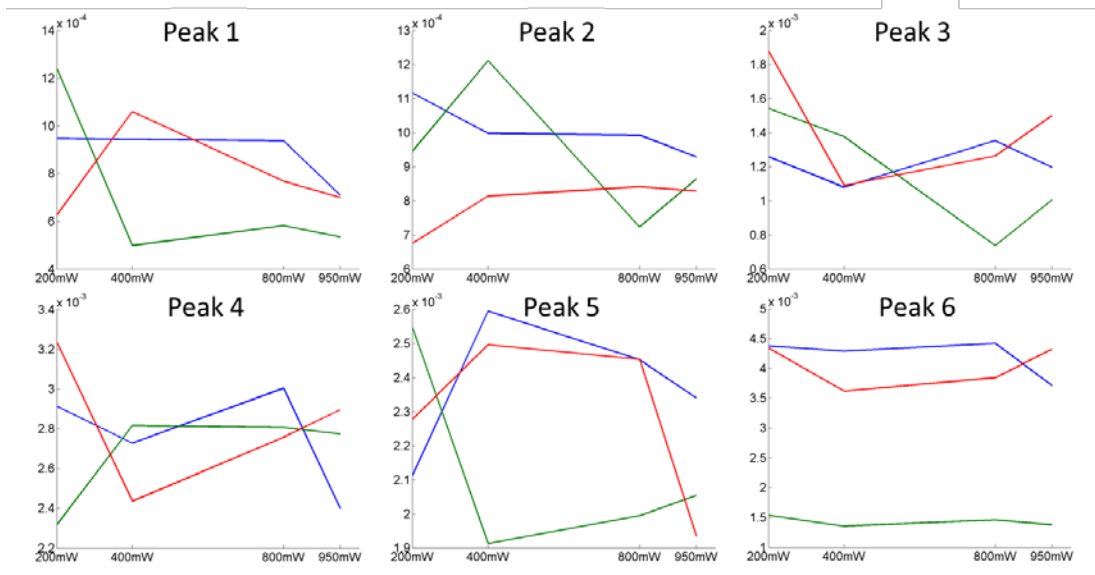


Figure 27 The peak heights for the Raman peaks identified in table 6 are plotted against the incident power levels. The blue lines are from the base glass, the green are from the grown glass, and the red are from the nucleated glass.

The below bandgap focused experiments had no observed topographical changes other than ablation craters which can also be seen with an optical microscope in figure 28. The purple circles around ablation craters are where marker dots were placed in order to be able to keep track of irradiated areas. Note though that the circle on the picture from the visible microscope for the grown sample is for an ablation crater that was created after the focused experiment was complete. The only condition that was able to show changes from the laser exposures was the 159mW power for the nucleated and grown samples. It appears that this area was near a threshold, since the entire area did not ablate. This could be partially due to the sample not being completely flat. The topographical changes on the samples should have been small enough to not be significant for a $2\mu\text{m}$ source. Other changes could have occurred, but were not able to be seen with the white light interferometer or visible microscope.

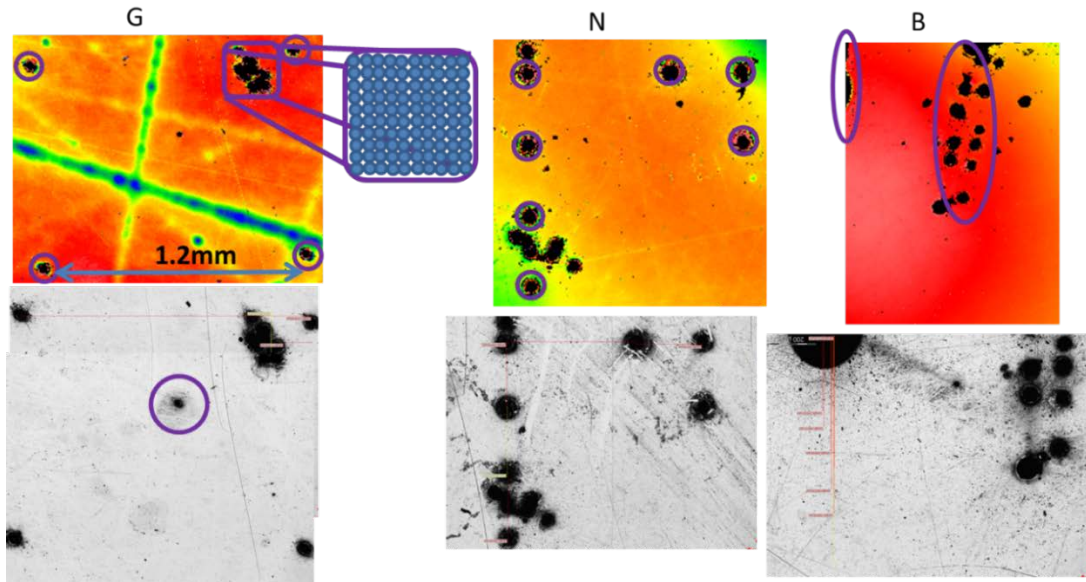


Figure 28 Visible microscopy and white light interferometry are shown for the focused exposures with the grown sample on the left, the nucleated sample in the middle, and the base sample on the right. No expansion is observed for any of the arrays, but ablation is seen for the highest power level in the grown and nucleated samples.

The above bandgap irradiation regime had very different results than the below bandgap regime. For these samples, photo-expansion was easily observed as seen in figure 29 [39], where the expanded region is slightly smaller than the beam waist that was used for the experiments. There also appear to be some surface cracks near the expansion, which could be from thermal stress. These cracks are not as prominent as some of those found in the threshold experiments.

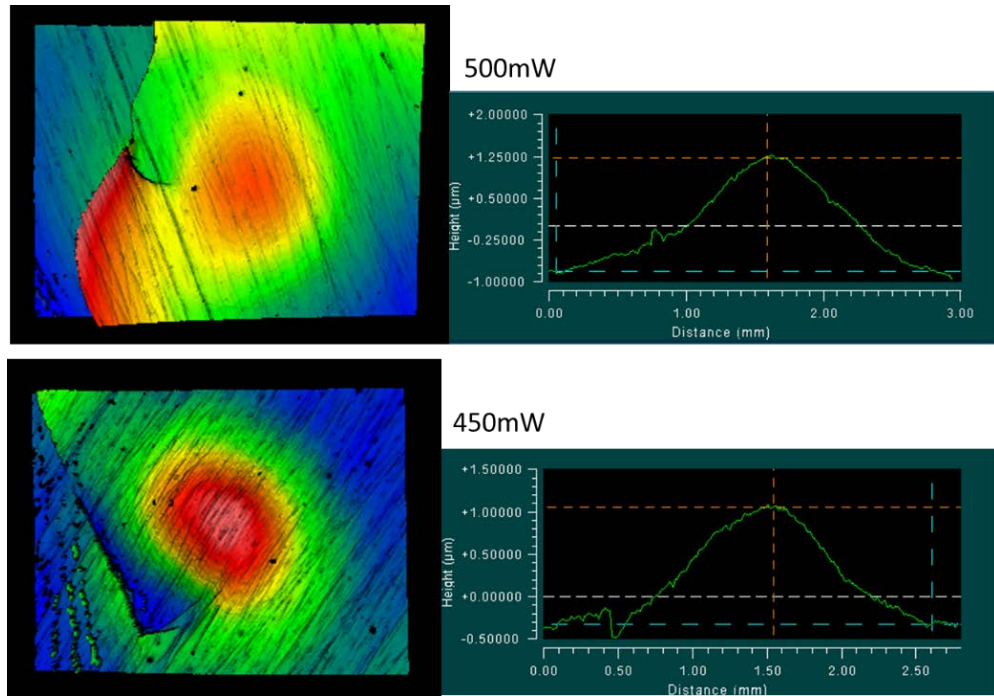


Figure 29 White light interferometry for the above bandgap irradiation experiments is shown for 500mW and 450mW exposures. Upper right image from [39].

4.5 Summary

Photo-modification of the chalcogenide glass specimens evaluated in the series of irradiation experiments was seen in both above and below bandgap exposure conditions. Above bandgap irradiation was applied to samples with a 488nm laser beam with a long focal length. The above bandgap case showed expansion that varied slightly with a change in average power.

Below bandgap irradiation was applied to samples with a laser beam of either focused or expanded 2 µm irradiation. A threshold map was also attempted for these materials. For the below bandgap case, various modifications were seen including melt pools, ablations craters with single or double halos, and expansion. The modifications with the below bandgap irradiation were not very consistent, which could be due to

inhomogeneities in the sample including compositional changes or growth of crystallites that change their local absorption coefficients.

5 COMPARISON OF COMPUTATIONAL TECHNIQUES WITH EXPERIMENTS

Once experiments were performed, computational models of heat distributions could be compared to experimental observations. Further modeling was performed with thermal properties of the compositionally similar commercial glass stated in chapter 2. These models were created in COMSOL Multiphysics with geometries that were either 2D-AS or 3D. These calculations followed the different experimental geometrical conditions and laser parameters that were used in the previous experiments. These comparisons were performed for the conditions used in the above bandgap, below-bandgap expanded beam, and below-bandgap threshold experiments. A comparison of calculated temperatures with observed changes in materials in experiments was performed, as well as a look into the stability of the results obtained. Additionally, the differences in the deviation for the above and below bandgap cases of the calculated temperature to the temperature one would expect for the various observed material modifications.

5.1 Comparison of Calculated Temperatures with Observed Material Changes

The above bandgap simulations were performed with both 3D and 2D-AS model geometries. The peak temperatures were looked at after the samples were irradiated for 100s for the above band gap case, which is when the temperature appears to be reaching a steady state. The power levels solved for were 450mW and 500mW, which were the same as the ones used in experiments. The calculated temperature distributions across the samples for the two power levels can be seen in figure 30.

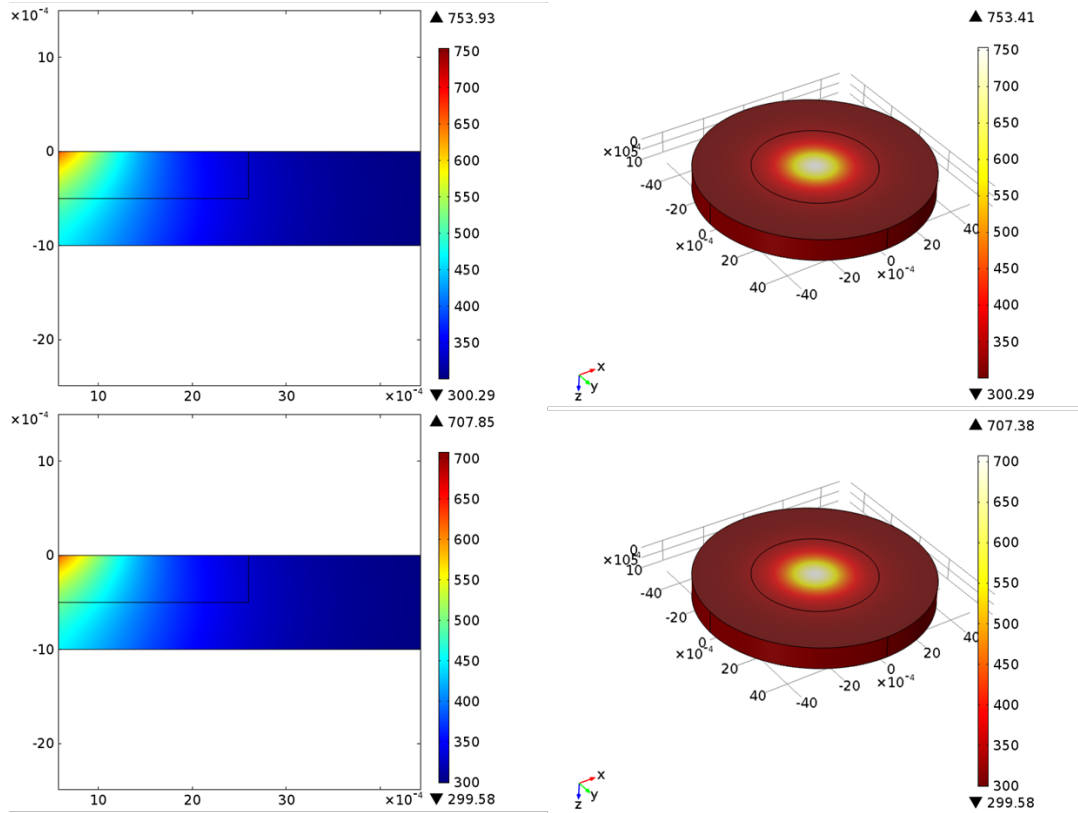


Figure 30 The temperature from simulations after 100s is shown for the 500mW (top row) and 450mW (bottom row) for the axially-symmetric and 3D simulations.

For these samples the maximum temperature reached was about 708K for the 450mW case, and 754mW for the 500mW case for both the 3D and 2D-AS geometries. These temperatures are several hundred degrees above both the glass transition and the crystallization temperature of the glass. The maximum temperature for these samples was also solved for using the semi-infinite material approximation. These calculations obtained values of 852.4K for the 500mW case, and 767.2K for the 450mW case, which were 60-100K larger than their respective finite boundary simulations.

The radius of the area where the temperature is above 513K, which is the crystallization temperature of the glass, is approximately 1mm in radius for the 500mW case and slightly below for the 450mW case. Additionally, the radius of the area where the temperature is above 481K, which is the glass transition temperature of the glass, is

approximately 1.2mm in radius for the 500mW case and slightly below for the 450mW case. For these experiments the incident laser beam radius was 1.3mm. Also the radius of the expanded region was approximately .6mm for the 500mW case and 0.5mm for the 450mW cases. The incident laser beam was larger than the area that should be above Tx according to the finite boundary model, which was in turn larger than the area that saw expansion.

Wide area exposures were investigated next. The samples for these were approximated as perfect quarter circles, since they were done on circular samples that were cut into four pieces. The samples that were used in the experiments though were all different sized pieces. In the simulations the laser was positioned radially 2.5mm from the tip of the wedge, and was centered on the sample azimuthally. The simulation included 200 pulses at a 20 kHz RR, which corresponds to 0.01s of irradiation time. As can be seen in figure 31, the maximum temperature reached was 293.19K for the highest power used, and 293.16K for the lowest power used. The starting temperature for these simulations was 293.15K, so both of these numbers are within the error of no temperature change for 200 pulses. The time of the irradiation in the experiment though was 5min, which would correspond to 6×10^6 pulses, so 200 pulses is not necessarily a very good indicator of the peak temperature that was reached in the sample. It did show though that there was a negligible temperature rise for short timescales.

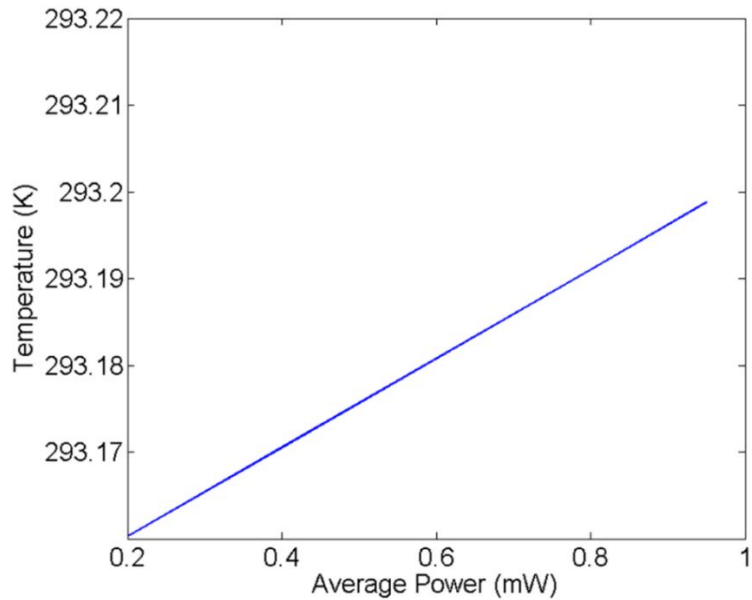


Figure 31 The maximum temperature for the different average incident powers for the wide area exposures is plotted. As can be seen there is a very small increase from the initial temperature of 293.13K.

Lastly the threshold conditions were modeled. Again 200 pulses were used, though in these simulations 1 kHz was used to match experiments which corresponds to 0.2s of exposure. This exposure time covers the 50ms exposures, and is relatively close to the 0.5s exposures. The simulations were performed with the focal point of the laser beam at different z positions. Each of the simulated points started at room temperature, and therefore neglects any residual heat that may be present from previous exposures that did not have time to fully dissipate. Figure 32 shows the peak temperatures that were reached for the varying focal positions for 30 and 40mW incident laser power.

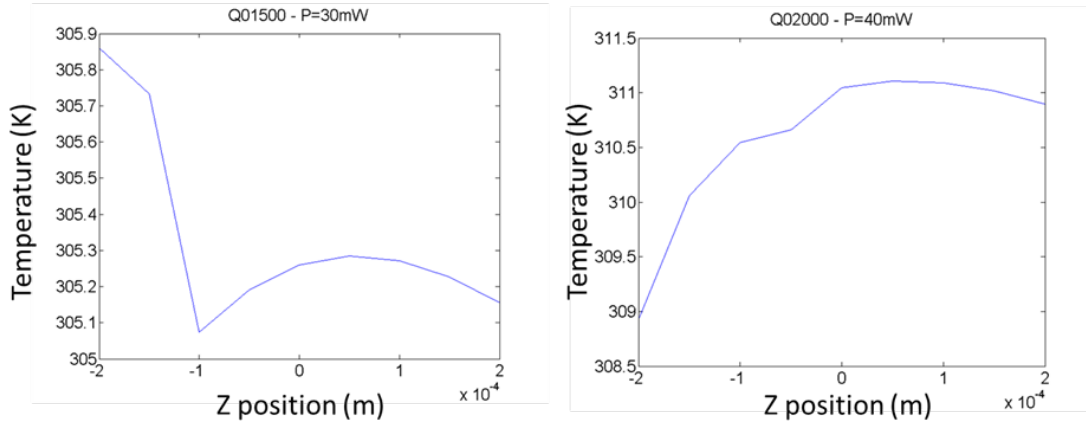


Figure 32 The maximum temperature reached for different z-positions of the focus of the laser for the threshold exposures is plotted for an incident power of 30mW on the left, and 40mW on the right.

These power levels are representative of some of the powers that were used in the experiment. As can be seen in the scales on the left, the temperature variation between these power levels was quite small, and can be considered within the error of the simulations that were performed. This would indicate that at least in the 50ms and .5s exposure regimes the different irradiated spots should have seen approximately the same temperature rise for the same power levels. Additionally, the temperature rise seen in the simulation was only 12-17°C, which one would not expect to create any noticeable changes for the timescales used in these experiments for thermal processes. Ablation and melt pools were seen in this conditions though, which one would not expect to see with the minimal temperature rise that was calculated. Since the properties used in the simulations were not quite those of the materials that were irradiated, simulations were performed to see if these differences could cause the discrepancies between the temperatures simulated and the material properties that were observed.

In order to determine whether small changes in the material and laser properties used in the simulations have a significant impact on the above bandgap experiment,

simulations were performed for 100s irradiations where the material properties including heat capacity, thermal conductivity, density, average power and beam waist were varied one at a time. The maximum temperatures found can be seen in figure 33.

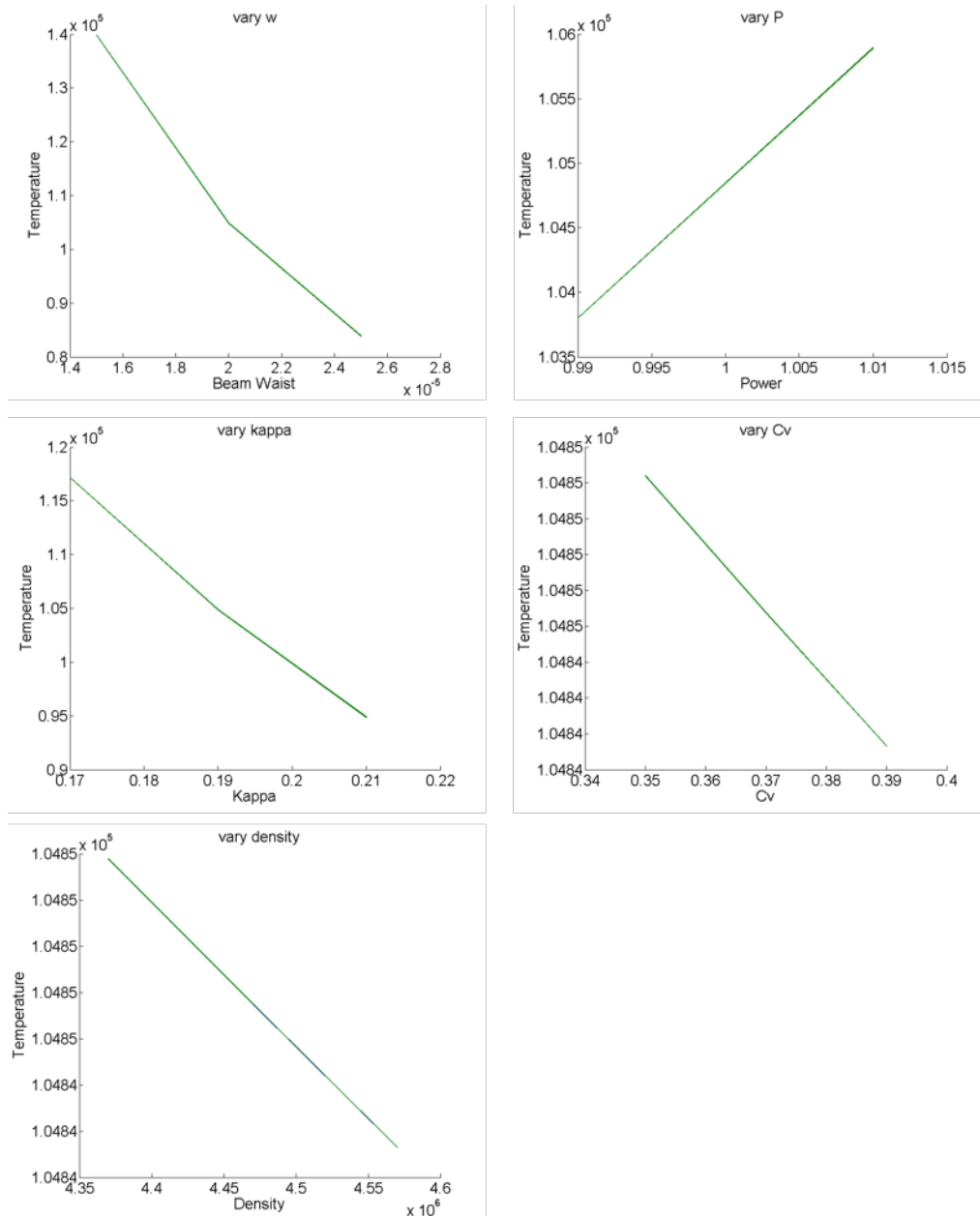


Figure 33 The maximum temperatures for variations in beam waist (top left), incident power (top right), thermal conductivity (middle left), heat capacity (middle right), and density (bottom left) are plotted for the above bandgap case. As can be seen the thermal conductivity and beam waist appear to have larger effects than the other parameters on the maximum temperature reached.

Looking at the changes from the uncertainty in the parameters, it is likely that thermal conductivity and laser beam waist are likely to have a more significant impact on the maximum temperature of the below bandgap simulations than the other properties that were varied.

In order to determine whether small changes in the material properties have a significant impact on the below bandgap focused experiments, simulations were done with 20 pulses where the material properties including heat capacity, thermal conductivity, reflection coefficient, and density were varied one at a time. The maximum temperatures found can be seen in figure 34.

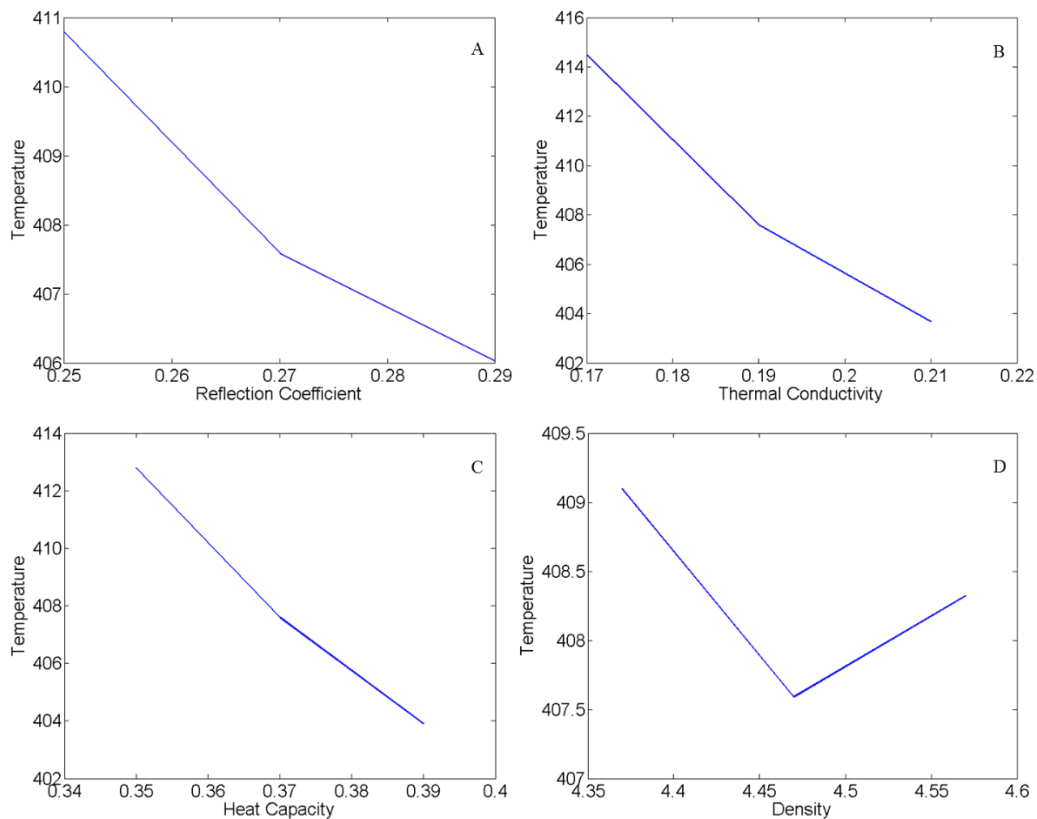


Figure 34 The maximum temperature for variations in the reflection coefficient (A), thermal conductivity (B), heat capacity (C), and density (D) are plotted for the below bandgap case. Of these the density has the least impact on the final attained temperature.

From looking at the changes from the uncertainty in the parameters, it is likely that thermal conductivity, heat capacity, and the reflection coefficient are likely to have a detectible impact on the maximum temperature of the below bandgap simulations. These parameters, not examined in detail for the custom glass of interest in this study, will be examined in more detail in future.

5.2 Differences in Deviation for Above and Below Bandgap

If one assumes that all of the material property changes occur from thermal processes, then the simulations that were performed did not match well with the material changes that occurred in the experiments. The trend of deviation though is different for the above and below bandgap irradiation cases. For the above bandgap case, the simulations predict a temperature that is much too high, 415-559°C, as compared to a glass transition temperature of 208°C and crystallization temperature of 240°C, while the below bandgap simulations predict a temperature that is much too low, nearly zero to around 20°C, as compared to a glass transition temperature of 208°C and crystallization temperature of 240°C. This data, in conjunction with the thermal properties of the glass found from its DSC curve can allow us to assess what changes occur at certain temperature conditions.

This could indicate that there are different processes occurring in these two regimes, or that the different types of heating are occurring for the two simulations. There are several factors that could contribute to the discrepancy including not accurate enough property data, error in measurement of laser parameters, errors in the simulation, neglecting phase changes in the simulation, neglecting additional local heating from

crystallites, and/or non-thermal processes could be occurring such as optically induced changes.

5.3 Summary

It has been shown that there is a deviation of the maximum temperature from the computational model predictions from what one would expect with the observed changes in the materials. This could be due to several factors including not accurate enough property data, error in measurement of laser parameters, errors in the simulation, neglecting phase changes in the simulation neglecting additional local heating from crystallites, and/or non-thermal processes could be occurring such as optically induced changes. Most of these though do not account for the magnitude of the observed discrepancies unless the values are much further from what were used than was anticipated.

6 CONCLUSION

This study has initiated the ground work to be able to determine the distribution of laser-induced heating and its associated effects on the multi-component ChG that was used in this study. The results from the simulations and experiments were compared in order to correlate simulated temperature increases with observed material modifications. As a result of the initial effort carried out in this thesis, a computational and experimental protocol has been developed which can aid in the interpretation of laser-induced modification in chalcogenide glasses suitable for glass ceramic formation based on their nucleation and growth attributes.

Two strategies to computationally model the laser-induced material modification were developed. The above bandgap and below bandgap laser irradiation needed different models, due to the differences in where and when the energy is deposited into the material. Additionally separate boundary condition models were created for the above bandgap in order to probe a semi-infinite material approximation in order to access its validity. Other approximations were also looked into for the simulations including the time steps the solver was using for the pulsed models, which lead to a determination of an associated uncertainty of the maximum obtained temperature.

Experiments were then performed. The first set of experiments involved using a 488nm CW laser for the above bandgap condition. This laser had a long focal length, so that there was not significant divergence near where the sample was. These exposures lead to expansion on the surface of the sample. The simulations of the same irradiation conditions though gave solutions that were several hundred degrees above both the glass transition temperature and the crystallization temperature.

Below bandgap irradiation was then performed with a 2 μ m laser in a ns pulsed regime. This experiment did not create any noticeable changes to the surface of the sample. Raman spectroscopy was also performed on these samples, and only minor changes could be observed. The simulations for these conditions lead to negligible temperature increases for 200 pulses. Focused pulses were then used in order to have a larger intensity on the surface. Ablation was able to be seen at certain irradiation conditions for these experiments, but was not very consistent.

A threshold map was then created to see what power levels could lead to certain changes. Some expansion and some ablation were seen on the samples. They did not appear in a predictable manner though, which could be evidence of inhomogeneities in the material. Simulation of these conditions showed that there should not have been a large enough temperature rise to give melting or ablation for 200 pulses, which corresponds to the timescales of 0.05ms and 0.5s. Both of these timescales though saw ablation and melting. One possibility for these occurrences is that some of the crystallites in the glass have an absorption around 2 μ m, and therefore have increased local heating.

Overall the simulations did not quite align with the material property changes that were seen. This could be due to inaccurate input property data for the simulations, though these small inaccuracies should not be able to account for some of the large variation between the simulations and experiment. This could be an indicator that some of the changes observed were from non-thermal processes.

6.1 Future Work

Future work still needs to be done in order to determine the changes in the material that will occur from a specific set of exposure conditions, but tools to do this have been

developed. Simulation tools have also been developed, though they still need to be refined in order to be able to better predict what temperature changes should be occurring in the materials that were used. Methods to determine what changes occurred in the experiments have also been developed. Additionally more uniform samples need to be developed in order to have the same material properties between irradiated areas and these properties need to be measured for this specific composition. Along with better property data, a better characterization of the 2 μ m laser performance is needed. Also a better characterization of which crystallite species are grown and what their optical properties are needs to be accomplished. Other pulse duration and RRs also need to be probed in order to determine the best dose of irradiation to induce the size and distribution of crystallization wanted.

APPENDIX A: IRG-24 DATA SHEET FROM SCHOTT GLASS

SCHOTT, your reliable solutions provider in the IR industry

Infrared Chalcogenide Glass IRG 24

Product Information

IRG 24 has excellent transmission in the SWIR, MWIR, & LWIR and has the lowest dn/dT of the IR series glasses. Physical properties such as low dn/dT and low dispersion enable optical engineers to design color corrected optical systems without thermal defocusing. IRG 24 is optimized for pairing within the family of IR glasses and with other IR materials to support cost effective and high performance optical designs. Furthermore, IRG 24 can be processed by conventional grinding and polishing, single point diamond turning, or molding to support low to high volume component level fabrication.



Typical Forms of Supply

Typical forms of supply are upon customer request. Maximum sizes up to Ø 100 mm and 150 mm length.

For sample parts we offer polished banks:

- Diameter: 10 to 100 mm
- Thickness: 5 to 30 mm

Constants of Dispersion Formulas (1.0–12.0 μm)	
B ₁	5.1485 - 1.6332 * e ^{0.0011394 * T/100}
B ₂	0.4872 + 1.8158 * e ^{0.0010888 * T/100}
B ₃	0.5144 + 0.0005 * e ^{0.022290 * T/100}
C ₁	0.0000
C ₂	1.2111 - 0.7776 * e ^{0.00074058 * T/100}
C ₃	31.9045 + 0.0885 * e ^{0.017224 * T/100}

Refractive Index as a function of both wavelength and temperature may be determined from the following relation

$$n^2(\lambda, T) - 1 = \frac{B_1(T)\lambda^2}{\lambda^2 - C_1(T)^2} + \frac{B_2(T)\lambda^2}{\lambda^2 - C_2(T)^2} + \frac{B_3(T)\lambda^2}{\lambda^2 - C_3(T)^2}$$

Material Properties	
Composition	Ge ₁₀ As ₄₀ Se ₅₀
Density	4.47 g/cm ³
Thermal Expansion	20.4 x 10 ⁻⁶ /K
Specific Heat	0.37 J/gK
Thermal Conductivity	0.18 W/mK
Transition Temperature	225 °C
Hardness (Knoop)	1.12 GPa
Fracture Toughness	0.347 MPa·m ^{3/4}
Shear Modulus	8.5 GPa
Young's Modulus	20.5 GPa
Thermal Change dn/dt @ 10.6 μm	19.9 x 10 ⁻⁶ /K

* For more information and questions please contact us

Wavelength μm	Refractive Index (@ 20 °C)
0.8	2.8030
0.9	2.7554
1.0	2.7249
1.5	2.6613
2.0	2.6414
3.0	2.6274
4.0	2.6221
5.0	2.6192
6.0	2.6170
7.0	2.6151
8.0	2.6132
9.0	2.6112
10.0	2.6090
11.0	2.6067
12.0	2.6040

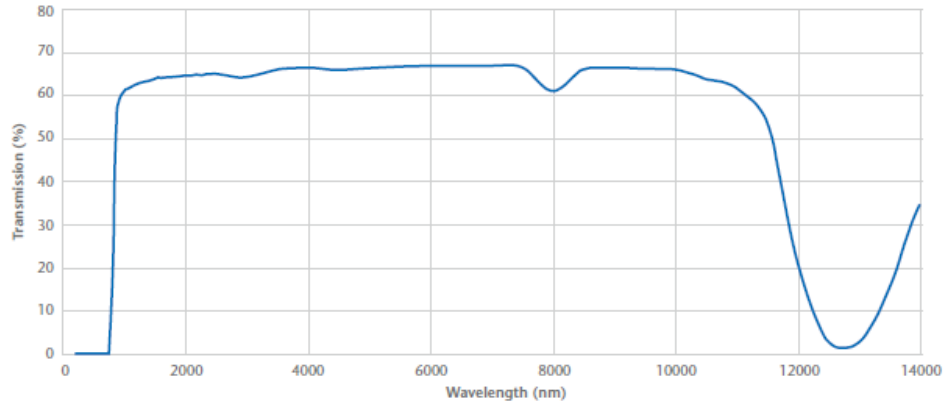
Temperature Coefficients of Refractive Index -55 to 75 °C*	
λ (μm)	Δn _w / ΔT [10 ⁻⁶ /K]
1.0	45.7
3.0	25.8
5.0	20.9
7.0	20.0
10.6	19.9
12.0	18.8



Figure 35 Schott data sheet for IRG 24.
http://www.schott.com/advanced_optics/english/download/schott-infrared-chalcogenide-glasses-irg24-october-2013-eng.pdf

Infrared Chalcogenide Glass IRG 24

Transmission of Infrared Glass IRG 24 with Thickness 10.0 mm (Typical Values)



NIR: 750 – 1400 nm	
Wavelength (nm)	Transmission T(%)
750	0.00
800	13.50
850	48.20
900	57.63
950	59.77
1000	60.95
1100	61.76
1200	62.52
1300	62.99
1400	63.37

SWIR: 1400 – 3000 nm	
Wavelength (nm)	Transmission T(%)
1400	63.37
1450	63.50
1550	64.03
1650	64.05
1750	64.23
1850	64.26
1950	64.48
2050	64.58
2150	64.62
2250	64.61
2350	64.78
2450	64.80
2500	64.81
3000	64.20

MWIR: 3000 – 5000 nm	
Wavelength (nm)	Transmission T(%)
3000	64.20
3500	65.92
4000	66.38
4500	65.84
5000	66.31

LWIR: 8000 – 14000 nm	
Wavelength (nm)	Transmission T(%)
8000	60.86
8500	65.93
9000	66.29
9500	66.10
10000	65.90
10500	63.80
11000	61.57
11500	53.49
12000	20.71
12500	2.41
13000	2.28
13500	15.02
14000	35.02

Version July 2013 | SCHOTT Advanced Optics reserves the right to make product changes in this product flyer without notice.



Advanced Optics
 SCHOTT AG
 Hattenbergstrasse 10
 55122 Mainz
 Germany
 Phone +49 (0)6131/66-1812
 Fax +49 (0)3641/2888-9047
 info.optics@schott.com
 www.schott.com/advanced_optics



Figure 36 Schott data sheet for IRG 24.
http://www.schott.com/advanced_optics/english/download/schott-infrared-chalcogenide-glasses-irg24-october-2013-eng.pdf

APPENDIX B: DOSAGES FOR THRESHOLD MAPPING

Table 7 Dosages for base glass threshold map in $\frac{Js}{cm^2}$. The dosages were calculated assuming the focus was at the surface of the sample in the middle of the vertical distance that was traveled.

time	50ms				
power (W)	0.038	0.035	0.032	0.030	0.028
z = -2E-4	0.275	0.253	0.235	0.218	0.206
z = -1.5E-5	0.286	0.263	0.244	0.227	0.214
z = -1E-4	0.295	0.271	0.252	0.234	0.221
z = -5E-5	0.300	0.276	0.256	0.238	0.225
0	0.302	0.278	0.258	0.240	0.226
z = 5E-5	0.300	0.276	0.256	0.238	0.225
z = 1E-4	0.295	0.271	0.252	0.234	0.221
z = 1.5E-4	0.286	0.263	0.244	0.227	0.214
z = 2E-4	0.275	0.253	0.235	0.218	0.206
z = 2.5E-4	0.262	0.241	0.223	0.208	0.196
time	.5s				
power (W)	0.034	0.032	0.029	0.028	0.026
z = -2E-4	2.495	2.347	2.127	2.045	1.913
z = -1.5E-5	2.598	2.444	2.215	2.129	1.991
z = -1E-4	2.677	2.518	2.282	2.193	2.052
z = -5E-5	2.726	2.564	2.324	2.234	2.090
0	2.743	2.580	2.338	2.248	2.103
z = 5E-5	2.726	2.564	2.324	2.234	2.090
z = 1E-4	2.677	2.518	2.282	2.193	2.052
z = 1.5E-4	2.598	2.444	2.215	2.129	1.991
z = 2E-4	2.495	2.347	2.127	2.045	1.913
z = 2.5E-4	2.375	2.234	2.024	1.946	1.820
time	1s				
power (W)	0.034	0.032	0.031	0.028	0.027
z = -2E-4	4.980	4.628	4.430	4.001	3.869
z = -1.5E-5	5.185	4.819	4.613	4.166	4.029
z = -1E-4	5.342	4.964	4.752	4.292	4.151
z = -5E-5	5.441	5.056	4.840	4.372	4.228
0	5.474	5.088	4.870	4.399	4.254
z = 5E-5	5.441	5.056	4.840	4.372	4.228
z = 1E-4	5.342	4.964	4.752	4.292	4.151
z = 1.5E-4	5.185	4.819	4.613	4.166	4.029
z = 2E-4	4.980	4.628	4.430	4.001	3.869
z = 2.5E-4	4.739	4.404	4.216	3.808	3.682

time	20s				
power (W)	0.034	0.032	0.030	0.028	0.026
$z = -2E-4$	99.819	93.222	86.845	81.128	76.510
$z = -1.5E-5$	103.926	97.058	90.419	84.466	79.659
$z = -1E-4$	107.073	99.997	93.156	87.024	82.071
$z = -5E-5$	109.054	101.847	94.880	88.634	83.589
0	109.731	102.479	95.469	89.184	84.108
$z = 5E-5$	109.054	101.847	94.880	88.634	83.589
$z = 1E-4$	107.073	99.997	93.156	87.024	82.071
$z = 1.5E-4$	103.926	97.058	90.419	84.466	79.659
$z = 2E-4$	99.819	93.222	86.845	81.128	76.510
$z = 2.5E-4$	94.992	88.714	82.646	77.205	72.811
time	10s				
power (W)	0.034	0.032	0.031	0.028	0.026
$z = -2E-4$	49.360	47.051	44.192	40.454	38.035
$z = -1.5E-5$	51.391	48.987	46.011	42.119	39.600
$z = -1E-4$	52.947	50.470	47.404	43.394	40.799
$z = -5E-5$	53.926	51.404	48.281	44.197	41.554
0	54.261	51.723	48.581	44.471	41.812
$z = 5E-5$	53.926	51.404	48.281	44.197	41.554
$z = 1E-4$	52.947	50.470	47.404	43.394	40.799
$z = 1.5E-4$	51.391	48.987	46.011	42.119	39.600
$z = 2E-4$	49.360	47.051	44.192	40.454	38.035
$z = 2.5E-4$	46.973	44.776	42.055	38.498	36.196

Table 8 Dosages for grown glass threshold maps in $\frac{Js}{cm^2}$. The dosages were calculated assuming the focus was at the surface of the sample in the middle of the vertical distance that was traveled.

time	50ms						
Power (W)	0.041	0.039	0.038	0.034	0.032	0.043	
z = -5E-5	0.321	0.309	0.297	0.273	0.255	0.339	
z = 0	0.323	0.311	0.298	0.274	0.256	0.341	
z = 5E-5	0.321	0.309	0.297	0.273	0.255	0.339	
z = 1E-4	0.315	0.303	0.291	0.268	0.250	0.333	
z = 1.5E-4	0.306	0.294	0.283	0.260	0.243	0.323	
z = 2E-4	0.294	0.283	0.272	0.250	0.233	0.310	
z = 2.5E-4	0.279	0.269	0.258	0.237	0.222	0.295	
z = 3E-4	0.264	0.254	0.244	0.224	0.209	0.279	
z = 3.5E-4	0.247	0.238	0.229	0.210	0.196	0.261	
z = 4E-4	0.231	0.222	0.214	0.196	0.183	0.244	
time	.5s						
Power (W)	0.031	0.032	0.034	0.037	0.039	0.041	
z = -5E-5	2.426	2.546	2.666	2.907	3.087	3.207	
z = 0	2.441	2.562	2.683	2.925	3.106	3.227	
z = 5E-5	2.426	2.546	2.666	2.907	3.087	3.207	
z = 1E-4	2.382	2.500	2.618	2.854	3.031	3.149	
z = 1.5E-4	2.312	2.426	2.541	2.770	2.942	3.056	
z = 2E-4	2.221	2.331	2.440	2.660	2.825	2.935	
z = 2.5E-4	2.113	2.218	2.322	2.532	2.689	2.793	
z = 3E-4	1.995	2.094	2.193	2.390	2.539	2.637	
z = 3.5E-4	1.872	1.965	2.057	2.243	2.382	2.474	
z = 4E-4	1.747	1.834	1.920	2.093	2.223	2.309	
time	1s						
Power (W)	0.037	0.038	0.041	0.034	0.032	0.029	0.027
z = -5E-5	5.873	6.053	6.414	5.453	5.092	4.612	4.252
z = 0	5.910	6.091	6.453	5.487	5.124	4.641	4.278
z = 5E-5	5.873	6.053	6.414	5.453	5.092	4.612	4.252
z = 1E-4	5.766	5.943	6.297	5.354	5.000	4.528	4.174
z = 1.5E-4	5.597	5.769	6.112	5.196	4.853	4.395	4.052
z = 2E-4	5.376	5.541	5.870	4.991	4.661	4.221	3.891
z = 2.5E-4	5.116	5.273	5.587	4.750	4.436	4.017	3.703
z = 3E-4	4.830	4.978	5.275	4.485	4.188	3.793	3.497
z = 3.5E-4	4.531	4.670	4.949	4.207	3.929	3.558	3.280
z = 4E-4	4.230	4.359	4.619	3.927	3.667	3.321	3.062

Table 9 Dosages for nucleated glass threshold mapping in $\frac{Js}{cm^2}$. The dosages were calculated assuming the focus was at the surface of the sample in the middle of the vertical distance that was traveled.

time	50ms					
power (W)	0.041	0.039	0.039	0.036	0.033	
z = -5E-5	0.324	0.309	0.309	0.285	0.261	
z = 0	0.326	0.311	0.311	0.286	0.262	
z = 5E-5	0.324	0.309	0.309	0.285	0.261	
z = 1E-4	0.318	0.303	0.303	0.279	0.256	
z = 1.5E-4	0.308	0.294	0.294	0.271	0.248	
z = 2E-4	0.296	0.283	0.283	0.261	0.239	
z = 2.5E-4	0.282	0.269	0.269	0.248	0.227	
z = 3E-4	0.266	0.254	0.254	0.234	0.214	
z = 3.5E-4	0.250	0.238	0.238	0.220	0.201	
z = 4E-4	0.233	0.222	0.222	0.205	0.188	
time	.5s					
power (W)	0.038	0.040	0.040	0.041	0.035	
z = -5E-5	3.027	3.147	3.147	3.267	2.786	
z = 0	3.045	3.166	3.166	3.287	2.804	
z = 5E-5	3.027	3.147	3.147	3.267	2.786	
z = 1E-4	2.972	3.090	3.090	3.208	2.736	
z = 1.5E-4	2.884	2.999	2.999	3.113	2.655	
z = 2E-4	2.770	2.880	2.880	2.990	2.550	
z = 2.5E-4	2.636	2.741	2.741	2.846	2.427	
z = 3E-4	2.489	2.588	2.588	2.687	2.292	
z = 3.5E-4	2.335	2.428	2.428	2.521	2.150	
z = 4E-4	2.180	2.266	2.266	2.353	2.007	
time	1s					
power (W)	0.038	0.038	0.040	0.036	0.033	
z = -5E-5	5.993	5.993	6.294	5.633	5.273	
z = 0	6.030	6.030	6.333	5.668	5.305	
z = 5E-5	5.993	5.993	6.294	5.633	5.273	
z = 1E-4	5.884	5.884	6.179	5.531	5.177	
z = 1.5E-4	5.711	5.711	5.998	5.368	5.025	
z = 2E-4	5.486	5.486	5.761	5.156	4.826	
z = 2.5E-4	5.220	5.220	5.482	4.907	4.593	
z = 3E-4	4.929	4.929	5.176	4.633	4.336	
z = 3.5E-4	4.624	4.624	4.856	4.346	4.068	
z = 4E-4	4.316	4.316	4.532	4.057	3.797	

time	10s					
power (W)	0.038	0.036	0.033	0.031	0.038	0.040
$z = -5E-5$	60.533	56.929	52.725	48.521	60.533	62.935
$z = 0$	60.909	57.283	53.053	48.822	60.909	63.326
$z = 5E-5$	60.533	56.929	52.725	48.521	60.533	62.935
$z = 1E-4$	59.433	55.895	51.767	47.640	59.433	61.792
$z = 1.5E-4$	57.686	54.252	50.246	46.239	57.686	59.976
$z = 2E-4$	55.406	52.108	48.260	44.412	55.406	57.605
$z = 2.5E-4$	52.727	49.588	45.926	42.264	52.727	54.820
$z = 3E-4$	49.785	46.821	43.364	39.906	49.785	51.761
$z = 3.5E-4$	46.705	43.924	40.681	37.437	46.705	48.558
$z = 4E-4$	43.593	40.998	37.970	34.943	43.593	45.323

REFERENCES

- [1] Seddon, A.B. "Chalcogenide glasses: a review of their preparation, properties and applications." *Journal of Non-Crystalline Solids*. 184. (1995): 44-50.
- [2] Meneghini, Chiara, and Alain Villeneuve. "As₂S₃ photosensitivity by two-photon absorption: holographic gratings and self-written channel waveguides." *J. Opt. Soc. Am. B*. 15.12 (1998): 2946-2950.
- [3] Tikhomirov, V.K. and V.M. Lyubin, "Novel photo-induced effects in chalcogenide glasses." *Journal of Non-Crystalline Solids*. 135.1 (1991): 37-48.
- [4] Petit, L, N Carlie, et al. "Effect of IR femtosecond laser irradiation on the structure of new sulfo-selenide glasses." *Optical Materials*. 29. (2007): 1075-1083.
- [5] Petit, Laeticia, et al. "Progress on the Photoresponse of Chalcogenide Glasses and Films to Near-Infrared Femtosecond Laser Irradiation: A Review." *IEEE JOURNAL OF SELECTED TOPICS IN QUANTUM ELECTRONICS*. 14.5 (2008): 1323-1334.
- [6] Zakery, A., and S.R. Elliott. "Optical properties and applications of chalcogenide glasses: a review." *Journal of Non-Crystalline Solids*. 330. (2003): 1-12.
- [7] Zoubir, Arnaud, Martin Richardson, et al. "Femtosecond direct writing of waveguides in non-oxide glasses." *Proc. of SPIE* . 5339. (2004): 175-184.
- [8] Tanaka, Keiji. "Midgap photon effects in As₂S₃ glass." *Philosophical Magazine Letters*. 84.9 (2004): 601-606.
- [9] Tanaka, Keiji, and Hisataka Hisakuni. "Photoinduced phenomena in As₂S₃ glass under sub-bandgap excitation." *Journal of Non-Crystalline Solids*. 198-200. (1996): 714-718.
- [10] Anderson, Troy. *FABRICATION OF INTEGRATED OPTOFLUIDIC CIRCUITS IN CHALCOGENIDE GLASS USING FEMTOSECOND LASER DIRECT WRITING*. Diss. the University of Central Florida, 2010
- [11] Ma, Hongli, Xianghua Zhang, and Jacques Lucas. "Infrared transmitting chalcogenide glass ceramics." *Journal of Non-Crystalline Solids*. 317. (2003): 270-274.
- [12] Floria, Catalin, Lynda Busse, et al. "A simple phenomenological study of photodarkening in As₂S₃ glasses." *Optical Materials*. 34. (2012): 1389-1393.
- [13] Zhang, X.H., L. Calvez, et al. "Infrared transmitting glasses and glass-ceramics." *Journal of Non-Crystalline Solids*. 352. (2006): 2411-2415.

- [14] Mecholsky Jun, J.J., C.T. Moynihan, P.B. Macedo, and G.R. Srinivasan. "Microstructure and properties of an infra-red transmitting chalcogenide glass-ceramic." *Journal of Materials Science*. 11. (1976): 1952-1960.
- [15] Massera, J, et al. "Nucleation and growth behavior of glasses in the TeO₂-Bi₂O₃-ZnO glass system." *Journal of Non-Crystalline Solids*. 356. (2010): 2947-2955.
- [16] Yinnon, H., and D.R. Uhlmann. "APPLICATIONS OF THERMOANALYTICAL TECHNIQUES TO THE STUDY OF CRYSTALLIZATION KINETICS IN GLASS-FORMING LIQUIDS, PART I: THEORY." *Journal of Non-Crystalline Solids*. 54. (1983): 253-275.
- [17] Morotta, A., A. Buri, and F. Branda. "Nucleation in glass and differential thermal analysis." *Journal of Material Science*. 16. (1981): 341-344.
- [18] Ray, Chandra, Kisa Ranasinghe, and Dilbert Day. "Determining crystal growth rate-type of curves in glasses by differential thermal analysis." *Solid State Sciences*. 3. (2001): 727-732.
- [19] Prieto-Alcon, R., J.M. Gonzalez-Leal, A.M. Bernal-Oliva, and E. Marquez. "Photo-amorphization and photo-oxidation of As Se thin films 50 50 deposited onto silicon substrates." *Materials Letters*. 36. (1998): 157-161.
- [20] Abdulhalim, I., R. Beserman, and R. Weil. "Photodarkening, structural instabilities, and crystallization of glassy As₂Se₃ induced by laser irradiation." *Physical Review B*. 40.18 (1989): 12476-12486.
- [21] Pribylova, H., K. Antonie, M. Vlcek, and H. Jain. "Kinetics of laser-induced photodarkening in arsenic based chalcogenide glasses." *Thin Solid Films*. 519. (2011): 3950-3953.
- [22] Stabl, M., and L. Tichy. "Photo-induced changes of the short wavelength absorption edge in some Ge-As-S amorphous thin films." *Optical Materials*. 27. (2004): 549-557.
- [23] Su, Xueqiong, Rongping Wang, Barry Luther-Davies, and Li Wang. "The dependence of photosensitivity on composition for thin films of GexAsySe1-x-y chalcogenide glasses." *Applied Physcis A*. 113. (2013): 575-581.
- [24] Tallman, R.E., B.A. Weinstein, et al. "Photo-crystallization in a-Se imaging targets: Raman studies of competing effects." *Journal of Non-Crystalline Solids*. 354. (2008): 4577-4581.
- [25] Peng, C., and M. Mansuripur. "Measurement of the thermal conductivity of erasable phase-change optical recording media." *Applied Optics*. 39.14 (2000): 2347-2352.
- [26] Horn, Alexander, Ilja Mingareev, et al. "Investigations on ultrafast welding of glass-glass and glass-silicon." *Applied Physics A*. 93. (2008): 171-175.

- [27] Horn, Alexander, Ilja Mingareev, and Alexander Werth. "Investigations on Melting and Welding of Glass by Ultra-short Laser Radiation." *Journal of Laser Micro/Nanoengineering*. 3.2 (2008): 114-118.
- [28] Richter, S., F Zimmermann, et al. "Ultrashort high repetition rate exposure of dielectric materials: laser bonding of glasses analyzed by micro-Raman spectroscopy." *Applied Physics A*. 110. (2013): 9-15.
- [29] Huang, Huan, Fangyuan Zuo, et al. "Fast phase transition process of Ge₂Sb₂Te₅ film induced by picosecond laser pulses with identical fluences." *Journal of Applied Physics*. 106. (2009): 63501-1-5.
- [30] Chang, C.M., C.H. Chu, et al. "Local electrical characterization of laser-recorded phase-change marks on amorphous Ge₂Sb₂Te₅ thin films." *Optics Express*. 19.10 (2011): 9492-9504.
- [31] Bechtel, J.H. "Heating of solid targets with laser pulses." *J. Appl. Phys.*. 46.4 (1975): 1585-1593.
- [32] Laurence, Ted, Jeff Bude, et al. "Metallic-like photoluminescence and absorption in fused silica surface flaws." *Applied Physics Letters*. 94. (2009): 151114-1-3.
- [33] Combis, Patrick, Philippe Cormont, et al. "Evaluation of the fused silica thermal conductivity by comparing infrared thermometry measurements with two-dimensional simulations." *Applied Physics Letters*. 101. (2012): 211908-1-4.
- [34] Hache, Alain, Phuong Anh Do, and Stefano Bonora. "Surface heating by optical beams and application to mid-infrared imaging." *Applied Optics*. 51.27 (2012): 6578-6585.
- [35] "Laser Heating - A Self Guided Tutorial" COMSOL Multiphysics Model Gallery <<http://www.comsol.com/model/laser-heating-a-self-guided-tutorial-12317>>
- [36] Choi, Jiyeon. Femtosecond laser written diffractive optical elements and their applications. Diss. University of Central Florida, 2010.
- [37] Le Harzic, R., N Huot, et al. "Comparison of heat-affected zones due to nanosecond and femtosecond laser pulses using transmission electronic microscopy." *Applied Physics Letters*. 80.21 (2002): 3886-3888.
- [38] Eaton, Shane, et al. "Heat accumulation effects in femtosecond laser written waveguides with variable repetition rate." *Optics Express*. 13.12 (2005): 4708-4716.
- [39] Siskin, Laura, Joshua Bradford, et al. "Distribution of Photo - Thermal Heating and Effects in Chalcogenide Glass." *Frontiers in Optics 2013/Laser Science XXIX*. (2013)

- [40] Gaida, C, M Gebhardt, et al. "Amplification of nanosecond pulses to megawatt peak power levels in Tm³ -doped photonic crystal fiber rod." OPTICS LETTERS. 38.5 (2013): 691-693.
- [41] Bridenbaugh, P.M., G.P. Espinosa, et al. "Microscopic origin of the companion A_i Raman line in glassy Ge(S,Se)₂." Physical Review B. 20.10 (1979): 4140-4144.
- [42] Georgiev, D.G., P. Boolchand, and M Micoulaut. "Rigidity transitions and molecular structure of As_xSe_{1-x} glasses." Physical Review B. 62.14 (2000): R9228-R9231.
- [43] Vodop'yanov, L.K., L.A. Fal'kovski, et al. "Raman scattering of light in a degenerate (Pb,Sn) Se semiconductor." JETP Letters. 53.11 (1991): 586-590.
- [44] Vassilev, V.S., Z.G. Ivanova, et al. "Glass-forming regions, properties, and structure of the chalcogenide As₂Se₃-GeSe₂-SnTe (Ag₄SSe) systems." Materials Letters. 59.1 (2005): 85-87.
- [45] Le Park, R, A. Piarristeguy, et al. "Ag-Ge-Se glasses: a vibrational spectroscopy study." Journal of Raman Spectroscopy. 44. (2013): 1049-1057.